DIEGO SERRANO RODRIGUEZ

TFM_DiegoSerranoRodriguez_MEI2025.pdf

Comprobación originalidad TFG/TFM (Moodle PP)

Turnitin TFG/TFM INDUS (Moodle PP)

Universidad Politecnica de Madrid

Detalles del documento

Identificador de la entrega

trn:oid:::1:3331820056

Fecha de entrega

7 sep 2025, 10:20 p.m. GMT+2

Fecha de descarga

7 sep 2025, 10:33 p.m. GMT+2

Nombre del archivo

164758_DIEGO_SERRANO_RODRIGUEZ_TFM_DiegoSerranoRodriguez_MEI2025_284053_1796850484.pdf

Tamaño del archivo

7.8 MB

105 páginas

17.372 palabras

86.151 caracteres

15% Similitud general

El total combinado de todas las coincidencias, incluidas las fuentes superpuestas, para ca...

Grupos de coincidencias

- **166** Sin cita o referencia 13%
  Coincidencias sin una citación ni comillas en el texto
- **11** Faltan citas 1%
  Coincidencias que siguen siendo muy similar al material fuente
- **13** Falta referencia 2%
  Las coincidencias tienen comillas, pero no una citación correcta en el texto
- **0** Con comillas y referencia 0%
  Coincidencias de citación en el texto, pero sin comillas

Fuentes principales

13% Fuentes de Internet
12% Publicaciones
5% Trabajos entregados (trabajos del estudiante)

Grupos de coincidencias

- **166** Sin cita o referencia 13%
  Coincidencias sin una citación ni comillas en el texto
- **11** Faltan citas 1%
  Coincidencias que siguen siendo muy similar al material fuente
- **13** Falta referencia 2%
  Las coincidencias tienen comillas, pero no una citación correcta en el texto
- **0** Con comillas y referencia 0%
  Coincidencias de citación en el texto, pero sin comillas

Fuentes principales

13% Fuentes de Internet
12% Publicaciones
5% Trabajos entregados (trabajos del estudiante)

Fuentes principales

Las fuentes con el mayor número de coincidencias dentro de la entrega. Las fuentes superpuestas no se mostrarán.

1	Internet	ricerca.univaq.it	3%
2	Internet	www.research-collection.ethz.ch	<1%
3	Internet	hal-mines-paristech.archives-ouvertes.fr	<1%
4	Publicación	Luigi Lombardi, Raffaele Raimondo, Giulio Antonini. "Electrothermal formulation ...	<1%
5	Internet	www.pes-publications.ee.ethz.ch	<1%
6	Internet	repository.charlotte.edu	<1%
7	Internet	repository.tudelft.nl	<1%
8	Internet	vbn.aau.dk	<1%
9	Trabajos del estudiante	Fachhochschule Kärnten Gemeinnützige Privatstiftung	<1%
10	Internet	arxiv.org	<1%

11 Internet

upcommons.upc.edu <1%

12 Internet

vtechworks.lib.vt.edu <1%

13 Internet

www.diva-portal.org <1%

14 Trabajos del estudiante

University of Huddersfield <1%

15 Internet

research-information.bris.ac.uk <1%

16 Internet

m.moam.info <1%

17 Publicación

Abdallah Kouzou. "Power Factor Correction Circuits", Elsevier BV, 2018 <1%

18 Internet

docslib.org <1%

19 Internet

ijeee.iust.ac.ir <1%

20 Internet

textarchive.ru <1%

21 Publicación

Dominik Koch, Hannes Bantle, Javier Acuna, Philipp Ziegler, Ingmar Kallfass. "Des... <1%

22 Publicación

Giulio Antonini, Daniele Romano, Luigi Lombardi, Albert Ruehli. "Partial element ... <1%

23 Internet

eldorado.tu-dortmund.de <1%

24 Internet

ltu.diva-portal.org <1%

25 Publicación

Ashraf B. Islam, Syed K. Islam, Fahmida S. Tulip. "Design and Optimization of Prin... <1%

26 Publicación

Georgios E. Sfakianakis, Jordi Everts, Elena A. Lomonova. "Overview of the require... <1%

27 Internet

mafiadoc.com <1%

28 Internet

etheses.whiterose.ac.uk <1%

29 Internet

journals.riverpublishers.com <1%

30 Internet

api.research-repository.uwa.edu.au <1%

31 Internet

trace.tennessee.edu <1%

32 Publicación

Giulio Antonini, Albert E. Ruehli, Daniele Romano, Fabrizio Loreto. "The Partial Ele... <1%

33 Internet

ebin.pub <1%

34 Internet

oa.upm.es <1%

35 Publicación

Stefan Quabeck, Lukas Braun, Niklas Fritz, Severin Klever, Rik W. De Doncker. "A ... <1%

36 Trabajos del estudiante

Universidad Politécnica de Madrid <1%

37 Trabajos del estudiante

University of South Australia <1%

38 Internet

phys.au.dk <1%

39 Internet
www.researchgate.net <1%

40 Publicación
Nabeel Arif, Hyun Chung. "Alternating current-gas metal arc welding for applicati... <1%

41 Publicación
Shahriar Jalal Nibir, Mehrdad Biglarbegian, Babak Parkhideh. "A Non-Invasive DC... <1%

42 Internet
vdocuments.pub <1%

43 Publicación
Michael Laumen, David Heidenberger, Niklas Fritz, Rik W. De Doncker. "Rogowski... <1%

44 Trabajos del estudiante
University of Malaya <1%

45 Internet
dspace.cvut.cz <1%

46 Internet
epdf.pub <1%

47 Internet
lib.dr.iastate.edu <1%

48 Trabajos del estudiante
Royal Holloway and Bedford New College <1%

49 Internet
l2ep.univ-lille1.fr <1%

50 Internet
www.politesi.polimi.it <1%

51 Publicación
Abhishek Kumar, Ramesh C. Bansal, Deng Yan, Praveen Kumar. "Microgrid Handb... <1%

52 Publicación
Tobias Funk, Bernhard Wicht. "Integrated Wide-Bandwidth Current Sensing", Spri... <1%

53 Internet
hdl.handle.net <1%

54 Internet
stellarium-gornergrat.ch <1%

55 Publicación
Dean G. Duffy. "Green's Functions with Applications", Chapman and Hall/CRC, 2019 <1%

56 Trabajos del estudiante
University of Hong Kong <1%

57 Publicación
Arsalan Najafi, Omid Homaee, Michal Jasinski, Mahdi Golshan, Zbigniew Leonowi... <1%

58 Publicación
Branislav Djokić. "The Design and Calibration of Rogowski Coils", NCSLI Measure, ... <1%

59 Publicación
Frank Vollmer, Deshui Yu. "Optical Whispering Gallery Modes for Biosensing", Spr... <1%

60 Publicación
Philipp Ziegler, Michael Bura, Jörg Haarer, Philipp Marx, David Hirning, Jörg Roth-... <1%

61 Publicación
Sunaina Rajora, Mansi Butola, Kedar Khare. "Calculating Numerical Derivatives u... <1%

62 Trabajos del estudiante
University of Strathclyde <1%

63 Publicación
Xiaoyu Liu, Hui Huang, Chaoqun Jiao. "Modeling and Analyzing the Mutual Induct... <1%

64 Internet
ir.ua.edu <1%

65 Internet
web.archive.org <1%

66 Trabajos del estudiante
RMIT University <1%

67 Internet

ndl.ethernet.edu.et <1%

68 Publicación

Ting, C.S.. "Stability analysis and design of Takagi-Sugeno fuzzy systems", Inform... <1%

69 Publicación

Yang Xue, Junjie Lu, Zhiqiang Wang, Leon M. Tolbert, Benjamin J. Blalock, Fred Wa... <1%

70 Internet

bayanbox.ir <1%

71 Internet

dokumen.pub <1%

72 Publicación

Péter Márton. "The principles of the complete measurement of an off-centred ele... <1%

73 Trabajos del estudiante

University of Leeds <1%

74 Internet

kth.diva-portal.org <1%

75 Internet

metrica.inrim.it <1%

76 Internet

tokyo-metro-u.repo.nii.ac.jp <1%

77 Publicación

Chucheng Xiao, Lingyin Zhao, T. Asada, W.G. Odendaal, J.D. van Wyk. "An overvie... <1%

78 Publicación

Hashmi, Ghulam, Matti Lehtonen, and Mikael Nordman. "Modeling and experime... <1%

79 Publicación

Jun Song Koh, Neelakantam Venkatarayalu. "Modeling, analysis and measureme... <1%

80 Trabajos del estudiante

University of Lincoln <1%

81 Publicación

Weili Guo, Guochun Xiao, Laili Wang. "A Compact Magnetoresistance-Rogowski H... <1%

82 Internet

amsdottorato.unibo.it <1%

83 Internet

core.ac.uk <1%

84 Internet

dx.doi.org <1%

85 Internet

ia801301.us.archive.org <1%

86 Internet

roma.sckcen.be <1%

87 Internet

www.coursehero.com <1%

88 Internet

www.mdpi.com <1%

89 Publicación

A.E. Ruehli, H. Heeb. "Circuit models for three-dimensional geometries including ... <1%

90 Publicación

Akos Ferenc Hegedus, Tamas Daboczi. "A High-Speed Current Sensing Method Ba... <1%

91 Publicación

Andrew J. Fleming, Kam K. Leang. "Design, Modeling and Control of Nanoposition... <1%

92 Publicación

Eby G. Friedman. "Properties of on-chip inductive current loops", Proceedings of t... <1%

93 Publicación

Hanjong Yoon, Younghoon Cho. "Application of the Rogowski Coil Current Sensor ... <1%

94 Publicación

Julian Endres, Tobias Haas, Alexander Pawellek, Vinicius Kremer, Roger Franchino... <1%

95 Publicación

Martin Stumpf, Fabrizio Loreto, Giuseppe Pettanice, Giulio Antonini. "Partial-indu... <1%

96 Publicación

Mauricio Rigoni, Joao Garcia, Artur Garcia, Pedro Da Silva, Nelson Batistela, Patric... <1%

97 Publicación

Stefan Schmidt. "Computational Modeling of Electromagnetic and Thermal Effect... <1%

98 Internet

digitalcommons.memphis.edu <1%

99 Internet

futur.upc.edu <1%

100 Internet

patents.justia.com <1%

101 Internet

pure.tudelft.nl <1%

102 Internet

repositorio.uam.es <1%

103 Internet

scholarbank.nus.edu.sg <1%

104 Internet

theses.hal.science <1%

105 Internet

vdoc.pub <1%

106 Internet

www.diva-portal.se <1%

107 Internet

www.eek.ee.ethz.ch <1%

108 Publicación

Gerber, Dominic, Thomas Guillod, Reto Leutwyler, and Juergen Biela. "Gate Unit ... <1%

109 Publicación

James D. Taylor. "Introduction to Ultra-Wideband Radar Systems", CRC Press, 2020 <1%

110 Publicación

Jürgen Wittmann. "Integrated High-Vin Multi-MHz Converters", Springer Science ... <1%

111 Publicación

Yu. L. Klimontovich, G. Pontecorvo. "Statistical Physics", Routledge, 2024 <1%

112 Publicación

"Next-Generation ADCs, High-Performance Power Management, and Technology ... <1%

113 Publicación

Pascal Samuel Niklaus, Dominik Bortis, Johann Walter Kolar. "Beyond 50 MHz Ban... <1%

114 Publicación

Soumyajit Mandal. "Power supplies and thermal management", Elsevier BV, 2026 <1%

115 Publicación

Unified Signal Theory, 2011. <1%

POLITÉCNICA

36

Escuela Técnica Superior de Ingenieros Industriales
Universidad Politécnica de Madrid

José Gutiérrez Abascal, 2. 28006 Madrid
Tel.: 91 336 3060
info.industriales@upm.es

www.industriales.upm.es

Diego Serrano Rodríguez

05 TRABAJO FIN DE MASTER

INDUSTRIALES

TRABAJO FIN DE MASTER

Analysis, Design, and Evaluation of PCB-Integrated Magnetic-Field-Based Current Sensors for Next-Generation Wide-Bandgap DC–DC Switched-Mode Power Supplies

TRABAJO FIN DE MASTER
PARA LA OBTENCIÓN DEL
TÍTULO DE MASTER EN
ELECTRÓNICA INDUSTRIAL

SEPTIEMBRE 2025

Diego Serrano Rodríguez

DIRECTORES DEL TRABAJO FIN DE MASTER:
Prof. Dr. Miroslav Vasic
Dr.techn. Goran Miskovic

INDUSTRIALES
ETSII | UPM

POLITÉCNICA

34

Universidad Politécnica de Madrid
Escuela Técnica Superior de Ingenieros Industriales

Máster en Electrónica Industrial

Analysis, Design, and Evaluation of PCB-Integrated Magnetic-Field-Based Current Sensors for Next-Generation Wide-Bandgap DC–DC Switched-Mode Power Supplies

54

TRABAJO FIN DE MASTER

Presentada para optar al título de **Máster en Electrónica Industrial** por:

Diego Serrano Rodríguez
Ingeniero Técnico Industrial, especialidad en Electrónica Industrial

Bajo la dirección de:
Prof. Dr. Miroslav Vasic
Dr.techn. Goran Miskovic

Madrid, Septiembre 2025

Executive Summary

This thesis investigates **PCB-integrated Rogowski coils** as low-cost, galvanically isolated current sensors suitable for WBG-based converters. Three coil topologies were designed, simulated using the finite element method (FEM), and fabricated for experimental characterization under small-signal and large-signal conditions. The results, validated against theoretical models, highlighted the relationship between geometry, mutual inductance, and sensing performance. The most promising design was integrated into two converter prototypes: a GaN buck operating in continuous conduction mode and a SiC boost power-factor-correction stage in critical conduction mode, confirming the sensor's suitability under realistic operating conditions. To support design decisions, a set of figures of merit (FoMs) was introduced, and practical guidelines were proposed for coil selection. Finally, a preliminary Partial Element Equivalent Circuit (PEEC) solver was implemented in Matlab, achieving results within 30% deviation from FEM simulations, thereby demonstrating feasibility for further refinement. The work combines modeling, simulation, prototyping, and validation and contributes a systematic workflow for developing PCB Rogowski coils for next-generation WBG converters.
Key words:PCB-Rogowski coil, high-bandwidth AC current sensing, isolated current sensing, PEEC method

34

Resumen Ejecutivo

99

En este trabajo fin de máster se investigan las bobinas Rogowski integradas en PCB, como sensores de corriente aislados de bajo coste, destinados para convertidores de potencia basados en dispositivos WBG. Tres diferentes topologías son diseñadas, simuladas mediante el método de elementos finitos (FEM) y posteriormente fabricadas para su caracterización experimental en condiciones de pequeña y gran señal. Los resultados, validados frente a modelos teóricos, destacaron la relación entre la geometría, la inductancia mutua y el rendimiento del sensor. El diseño más prometedor se integró en dos prototipos: un convertidor Buck basado en GaN operando en modo de conducción continua y un convertidor Boost de corrección del factor de potencia (PFC) basado en SiC operando en modo de conducción crítica. Para facilitar la selección de diseños, se proponen distintas figuras de mérito (FoMs) y pautas de diseño. Finalmente, se implementó en Matlab un solver preliminar basado en el método PEEC (Partial Element Equivalent Circuit), que logró resultados con una desviación inferior al 30% respecto a las simulaciones FEM, demostrando así su viabilidad. Este trabajo combina modelado, simulación, prototipado y validación. Aporta un flujo de trabajo sistemático para el desarrollo de bobinas de Rogowski integradas en PCB destinadas a convertidores WBG de nueva generación.
Palabras clave:PCB-Rogowski coil, high-bandwidth AC current sensing, isolated current sensing, PEEC method

Abstract

The adoption of wide-bandgap (WBG) power semiconductors such as silicon carbide (SiC) and gallium nitride (GaN) is enabling a new generation of high-efficiency, high-frequency, and high-power-density converters. To fully exploit the capabilities of these devices, accurate and high-bandwidth current sensing is essential. Such sensing provides galvanic isolation, enables real-time health monitoring of converters, and allows control loops to operate with improved dynamic performance.

This thesis investigates PCB-integrated Rogowski coils as low-cost, high-bandwidth, galvanically isolated current sensors for DC–DC power converters. Three different coil topologies were designed, simulated, and experimentally characterized. Finite element method (FEM) simulations were employed to evaluate mutual inductance and parasitics, while fabricated prototypes were tested under small-signal and large-signal conditions to extract their equivalent circuit parameters and validate simulation results.

A comprehensive comparison between designs was carried out, leading to the selection of the most suitable topology for application-level validation. The chosen sensor was integrated into two representative WBG-based converter prototypes: a GaN buck converter in continuous conduction mode and a SiC boost power-factor-correction converter in critical conduction mode. These experiments confirmed the sensor's ability to accurately track switching currents under realistic operating conditions.

To guide future sensor development, a set of figures of merit (FoMs) was proposed, providing design-oriented metrics for sensitivity, bandwidth, insertion inductance, and common-mode rejection. Furthermore, a preliminary Partial Element Equivalent Circuit (PEEC) solver was implemented in Matlab to estimate the mutual inductance of PCB Rogowski coils. Despite its simplified formulation, the solver achieved results within 30% deviation from FEM simulations, validating its feasibility and potential for further refinement.

This thesis combines theoretical modeling, electromagnetic simulation, hardware prototyping, and system-level validation. The contributions include:

- A systematic workflow for the design and evaluation of PCB Rogowski coils.

- Experimental characterization of three coil topologies, with validation against FEM simulations.
- Integration and testing of the selected sensor in two WBG power converter prototypes.
- Introduction of figures of merit to compare coil designs and guide sensor selection.
- Development of a feasibility-stage PEEC solver for mutual inductance extraction.

The results demonstrate the relevance of PCB Rogowski coils as compact, accurate, and cost-effective sensors for WBG converters, and open avenues for future research on enhanced modeling and common-mode noise mitigation.

Thesis outline

The thesis is organized into five main chapters and supporting appendices:

- **Chapter 1 – Introduction**: Motivates the need for high-bandwidth current sensing in WBG power converters, identifies desirable sensor characteristics, and compares existing sensing technologies. A review of state-of-the-art PCB Rogowski coils is presented to establish the scope of research.
- **Chapter 2 – Rogowski Coils**: Introduces the operating principle, lumped-element modeling, and frequency response of Rogowski coils. The three topologies under study are described, along with the design workflow and experimental procedures. Simulation and measurement results are compared and discussed.
- **Chapter 3 – Sensor Realization**: Discusses the sensor manufacture and sensitivity characterization from the selected Rogowski coil topology. The effect of the total impedance introduced into the power loop is also addressed.
- **Chapter 4 – Experimental Validation**: The manufactured sensor is integrated into two WBG converter prototypes (a GaN buck and a SiC boost PFC). The sensor's behavior is evaluated

under realistic switching conditions, demonstrating its suitability for high frequency-ripple current sensing.

- **Chapter 5 – Figures of Merit & Design Guidelines**: Proposes a set of figures of merit (FoMs) for performance comparison among different Rogowski coil designs. Based on simulation and experimental results, practical guidelines are derived for a given PCB Rogowski coil structure design.
- **Chapter 6 – PEEC Modeling**: Provides an introduction to Partial Element Equivalent Circuit (PEEC) theory. A simplified Matlab-based solver is developed and applied to a given PCB Rogowski coil structure. Results are compared to FEM simulations and experimental data, highlighting feasibility and limitations.
- **Chapter 7 – Conclusions and Future Work**: Summarizes the main findings of the thesis. Directions for future work are outlined.
- **Appendices**: Contain supporting material including Matlab PEEC code, mathematical derivations and additional details on Rogowski coils applied to pulse-tracking.

12

Contents

Chapter 1 Introduction **11**

1.1 Framework **11**

1.2 Review of current sensing technologies **12**

1.3 Embedded Rogowski Coils in the SoA **16**

Chapter 2 Rogowski Coils **22**

2.1 Rogowski coils as current sensors **22**
2.1.1 Operating Principle of the Rogowski Coil . . . 22
2.1.2 Lumped Electrical Model and Frequency Response 23

2.2 Researched geometries **26**

2.3 Characterization of the designed PUCs **29**
2.3.1 On the PUC's winding resistance 34

2.4 Results **35**

Chapter 3 Sensor Realization **38**

3.1 Main constraints of the designed sensor **38**

3.2 Gain measurement **38**

3.3 Designed sensor **41**

3.4 Discussion on the impedance inserted into the power loop **42**

Chapter 4 Experimental Validation **45**

4.1 Researched converter topologies for PUC validation **45**
4.1.1 SiC PFC Boost converter 46
4.1.2 GaN Buck converter 50
4.1.3 Comment on the nature of the ringing 52

Chapter 5 Figures of Merit & Design Guidelines **57**

5.1 Motivation **57**

5.2 Proposed metrics to compare pick-up coils **57**

5.3 Design guidelines for coplanar pick-up coils **59**
5.3.1 General constraints 60
5.3.2 Sensed conductor width influence on the mutual inductance 64

Chapter 6 PEEC Modeling **67**

6.1 Motivation **67**
6.1.1 H field of an infinite strip with finite-width . . 67
6.1.2 Statement 69

6.2 The PEEC method **70**
6.2.1 Framework 72
6.2.2 Time domain PEEC formulation 72
6.2.3 Frequency domain PEEC formulation 75

6.3 Procedure to solve **76**
6.3.1 Partial inductances 77
6.3.2 Inductance formula for Manhattan geometries 78

6.4 Suggested simplified PEEC algorithm **79**
6.4.1 Results 82

13 **Chapter 7 Conclusions and Future Work** **85**

7.1 Contributions and alignment with SDGs **85**
7.1.1 Future Research Lines 86

Chapter 8 Appendix A: On the tracking of pulses 90

Chapter 9 Appendix B: Review of concepts applied in PEEC 93

Chapter 10 Appendix C: Matlab Code for Simplified PEEC 96

1

Introduction

Executive Summary

This chapter introduces the motivation and scope of the thesis. Reviews current sensing technologies and identifies embedded Rogowski coils as a promising alternative. **Main topics covered:**

- Motivation for high-bandwidth isolated current sensing.
- Comparison of existing sensing technologies.

1.1 Framework

Growing demand across all sectors—from utility-scale renewables and electric vehicles to consumer electronics and data centers —requires highly efficient, compact power converters that shrink bulky passive components. Wide-bandgap materials like SiC and GaN have intrinsic properties —higher critical electric field, wider bandgap, and superior thermal conductivity—that let them handle higher voltages and temperatures while switching faster than silicon. Given the demands for very-high switching frequency, power density, and efficiency, reliable operation of the entire power stage requires high-bandwidth current sensing. Such sensing enables continuous health monitoring of the converter and its components and expands control loops' bandwidth for improved dynamic performance. By employing non-invasive measurements, auxiliary and control circuits are shielded from hazardous events and the operating and transient voltages of the power stage—ideally without any energy dissipation. Among magnetically coupled approaches, PCB integrated Rogowski coils have drawn increasing attention for measuring fast AC currents by sensing the time-varying magnetic field around the conductor. They offer inherent galvanic isolation, high bandwidth,

excellent linearity, low cost, and seamless converter integration, while PCB implementation enables precise control of parasitic impedance.

1.2 Review of current sensing technologies

The adoption of wide bandgap (WBG) power semiconductor devices in modern power electronic converters enables significant advancements in switching frequency, efficiency, and power density [1-3]. These devices support the development of compact, highly dynamic systems with fast transient response characteristics. To fully leverage the benefits of WBG technology, accurate high-bandwidth current and voltage sensing is essential. These measurements play a critical role in enabling the fast, high-performance control loops required for effective regulation [4] and real-time health monitoring of power converters [5].

Current sensing solutions must be selected to meet a range of demanding criteria dictated by application-specific requirements. Among the most critical are [1]:

1. **Galvanic isolation** — necessary for safely measuring currents at floating potentials.
2. **Minimal impedance insertion within the power loop** — vital for maintaining energy efficiency and avoiding signal distortion.
3. **High immunity to common-mode (CM) noise** — essential in the presence of the high dv/dt transients characteristic of WBG switching.
4. **Compact form factor** — for integration into space-constrained designs.
5. **High measurement accuracy and linearity**.
6. **Low cost**.

[1] Power-consumption has been neglected but it is a major concern for very low-power ($< 5W$) applications which are out of the scope of this thesis

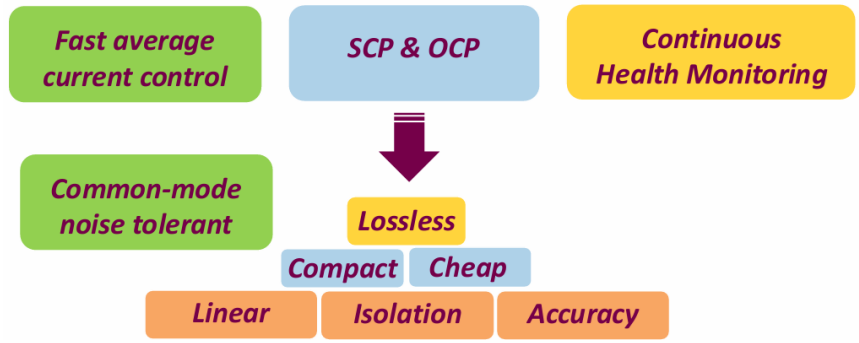

Figure 1: Applications and desirable features of high-bandwidth current sensor.

Several current sensing technologies are available, each with their inherent trade-offs. Some of the most popular technologies are among the following.

- **Hall-effect sensors** [**6,7**]]: Widely used for their DC sensing capability and inherent isolation. However, they suffer from limited bandwidth, core saturation, and size constraints.
- **Magneto-resistive sensors** [**8**]]: Offer high precision, DC sensing capability, and high CM immunity, but their relatively narrow bandwidth and bulk limit their suitability for MHz-range applications.
- **Current transformers (CTs)** [**9,10**]]: Provide excellent bandwidth and accuracy for AC current sensing, often exceeding tens of MHz. However, they cannot measure DC and are limited by core saturation and physical size.
- **Shunt resistors** [**11,12**]: Compact and capable of measuring both AC and DC currents. They do not provide isolation and exhibit degraded performance at high frequencies due to the skin effect and parasitic inductance.

39

Technology	Bandwidth	DC Capability	Sensitivity	Saturation	Linearity	Isolation
Hall	<250 kHz	Yes	High	Yes	Poor	Yes
GMR	<1 MHz	Yes	Very-high	Yes	Good	Yes
CT	<1 MHz	No	Very-high	Yes	Good	Yes
Shunt	<2 GHz	Yes	High	No	Poor	No
Rogowski	<3 GHz	No	Low	No	Excellent	Yes

Table 1: Comparison of Current Sensing Technologies

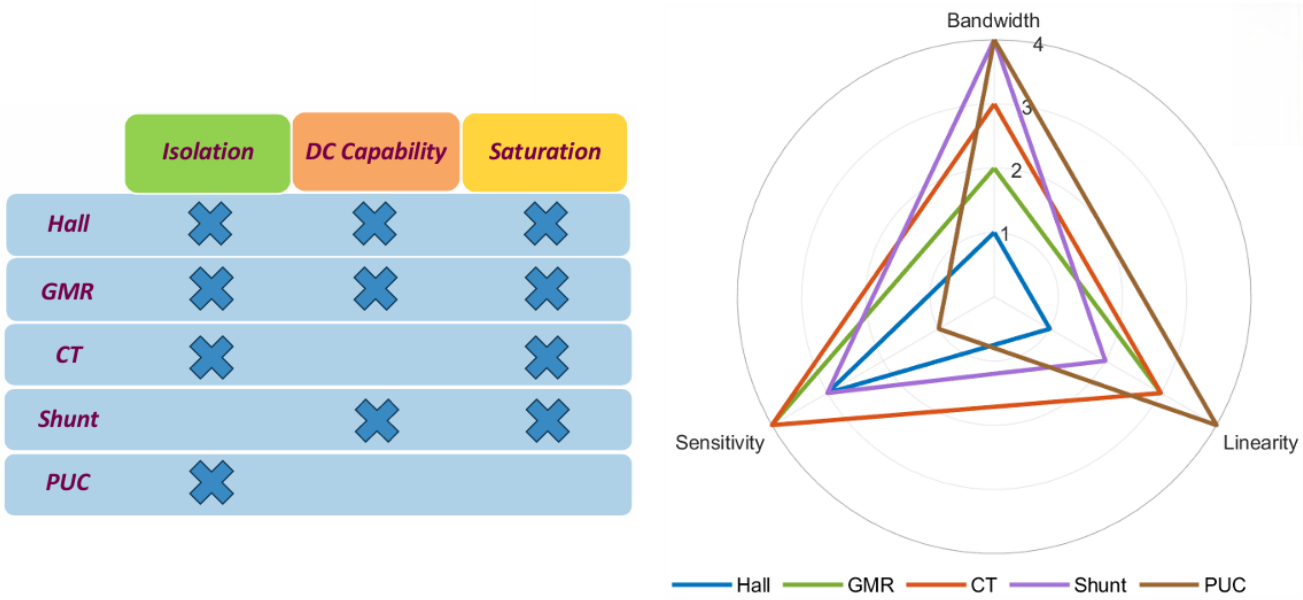

Figure 2: Comparison between several current sensing technologies.

Thereby, another promising approach is the use of embedded Rogowski coils [4,15-22]. These sensors are magnetic current-to-voltage transducers that are used in applications that require isolated measurement of alternating currents with a high bandwidth. They operate on the basis of the law of magnetic induction. Thus, they inherently provide galvanic isolation. The voltage at the sensor's secondary terminals depends on the derivative of the current through the primary conductor and the mutual inductance between it and the adjacent conductor. This magnetic coupling characteristic enables noninvasive alternating current measurement. The surrounding air serves as the main medium for the propagation of the magnetic field between the conductors. Consequently, because of the absence of a magnetic core, the sensor exhibits high linearity and low thermal drift within its operating range. The sensitivity of magnetically coupled sensors is mainly dependent on their mutual inductance ratio, M . In the case of Rogowski coils, due to the absence of a core, the magnitude of the coupling ratio is low, which limits their application in low-frequency current measurement. Since the voltage induced at the sensor terminals corresponds to the rate of change of the current over time, this voltage must be integrated to obtain an accurate reconstruction of the measured current. The PCB

implementation of this kind of sensors offers the opportunity for tight parasitics control, while achieving small form factors which ease their deployment in power converters.

1.3 Embedded Rogowski Coils in the SoA

Several studies have demonstrated the design and integration of Rogowski coils tailored for high-frequency current sensing. Rogowski coils were suggested to extend the bandwidth of magnetic sensors for non-intrusive current measurement. Their performance was evaluated to measure switching losses in power semiconductor devices [**?**]. In [20] a Rogowski coil-based short circuit protection circuit for high voltage discrete IGBT modules is presented.

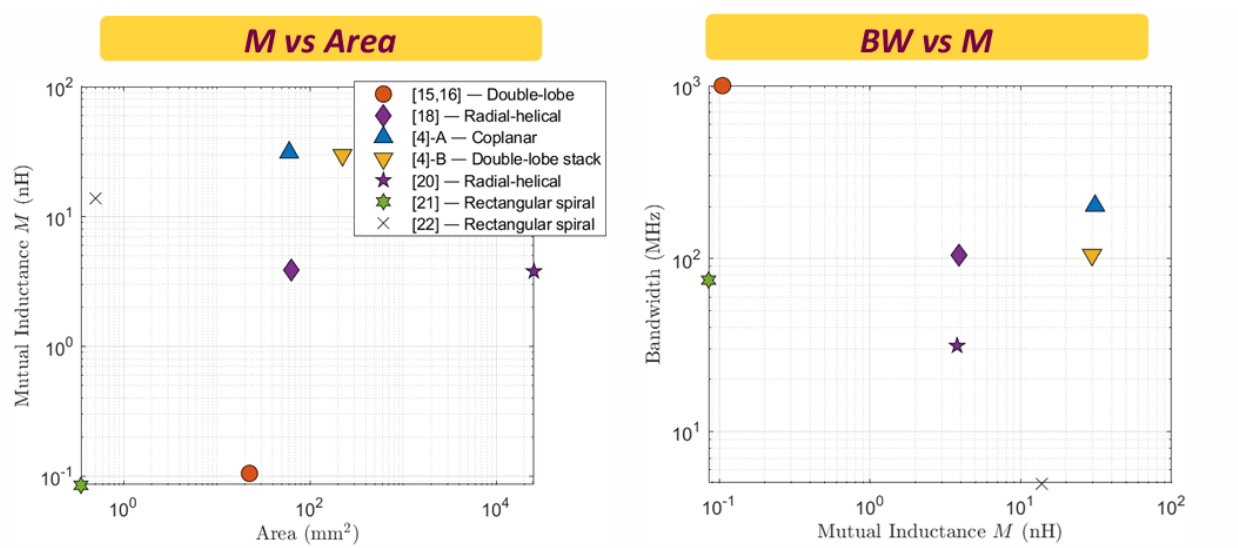

Figure 3: Comparison of different Rogowski coils found in the SoA.

Design	Area (mm^2)	Reported M (nH)	$L_{insertion}$ (pH)	BW (MHz)	Geometry
[15,16]	22.5	0.105	200	1000	Double-lobe
[17]	450	–	–	1	Coplanar
[18]	63.6	3.89	–	105	Radial-helical
[4]	60	31.1	–	202	Coplanar
[4]	224	29.7	–	105	Double-lobe stack
[20]	25320	3.78	–	31.3	Radial-helical
[21]	0.35	0.085	–	75	Rectangular spiral
[22]	0.5	13.79	–	5	Rectangular spiral

Table 2: Comparison of Embedded Rogowski Coil Designs

turnitin Página 28 de 116 - Engrega de integridad Identificador de la entrega trn:oid:::1:3331820056

In [15,16], a minimal-footprint 400 MHz AC current sensor is designed to overcome the intrinsic loading and signal distortion introduced by passive probes and shunt resistor parasitics within the switching node. The sensor's winding resembles an infinite-like geometry, where the sensed conductor is placed between each lobe. Different demonstrators compare the impact on the loop inductance of the switching node using a standalone custom Rogowski sensor versus off-the-shelf shunts and SMA connectors, while evaluating current sensing fidelity. Results demonstrate high-precision measurements with minimal post-processing and extremely low inductance insertion, outperforming shunt resistors under pulsed current testing.

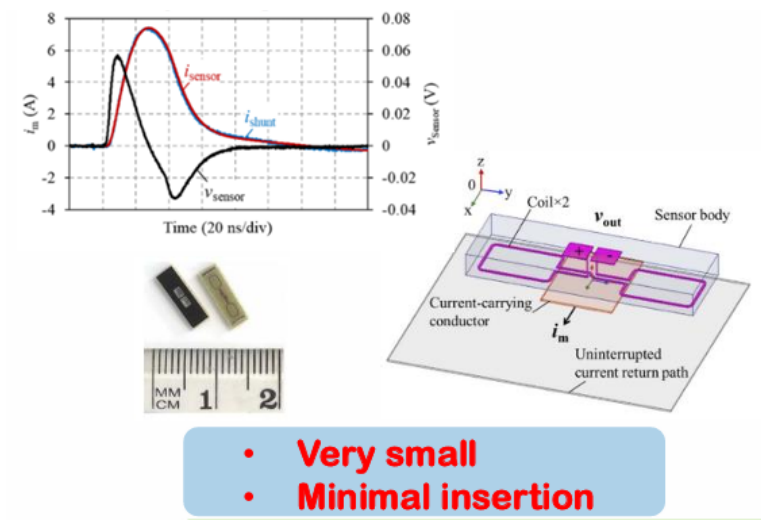

Figure 4: Sensor developed in [15,16].

In [17], a coplanar pick-up coil is developed to mitigate susceptibility to external magnetic fields and the low magnetic coupling inherent to planar Rogowski sensors. A prototype, where the main conductor wraps around the embedded sensing winding, is evaluated. A compact etched sensor is tested against arbitrary waveforms and compared to the voltage drop across a shunt resistor. After validating waveform fidelity, an alternative layout using a square spiral inductor placed beside the conductor is investigated. FEM analysis reveals this later geometry is more prone to external field interference and offers lower sensitivity compared to the coplanar arrangement.

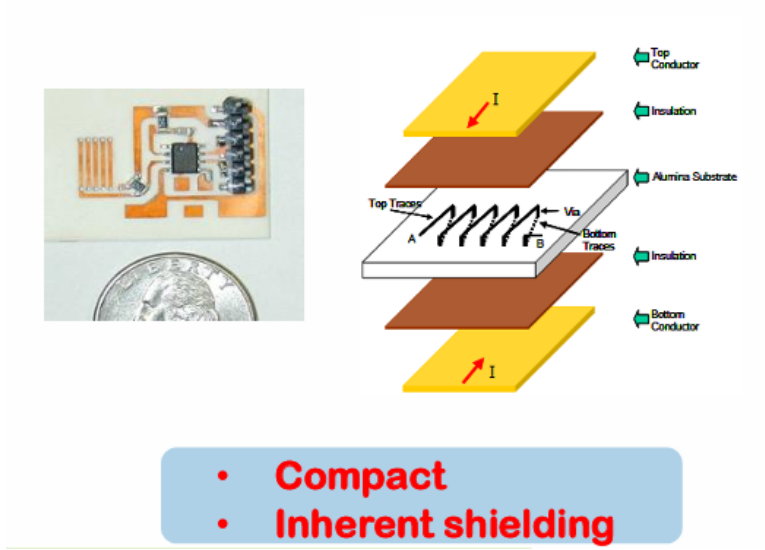

Figure 5: Sensor developed in [17].

In [18], an embedded 4 mm diameter Rogowski coil built around a via and placed directly within the power loop (in the switch node) is presented. To address common-mode disturbances, a fully differential design is proposed, employing a center-tap connection in the coil winding. Both single-ended and differential implementations are tested via double-pulse testing. The differential realization exhibits improved signal-to-noise ratio (SNR) due to enhanced common-mode rejection ratio (CMRR).

In [4], a feasibility study is conducted on integrated Rogowski coils for sensing the large signal 1.6 MHz inductor ripple current of an interleaved flying-capacitor RF amplifier. The work extends low-bandwidth commercial isolated sensors, such as those based on [19], by evaluating various Rogowski geometries: the coplanar coil of [18], the stacked layout from [15,16], and a traditional Rogowski design. Bandwidth, output impedance, mutual inductance, and susceptibility to common-mode coupling (when placed nearby a switching node or after the filter inductor) are reported. Despite their superior bandwidth and linearity, Rogowski coils are noted to underperform in CMRR compared to state-of-the-art current transformers (CTs).

In [20], a Rogowski-based short-circuit detection circuit for a 4.5 kV press-pack IGBT is developed. Using the Partial Element Equiva-

lent Circuit (PEEC) method, several compensation and return winding schemes are evaluated to improve SNR. The mutual coupling and output impedance are analyzed based on busbar orientation. Short-circuit tests demonstrate a reliable 500 ns turn-off delay post-SCP threshold exceedance, with only 10% overcurrent at a 4 kA nominal current.

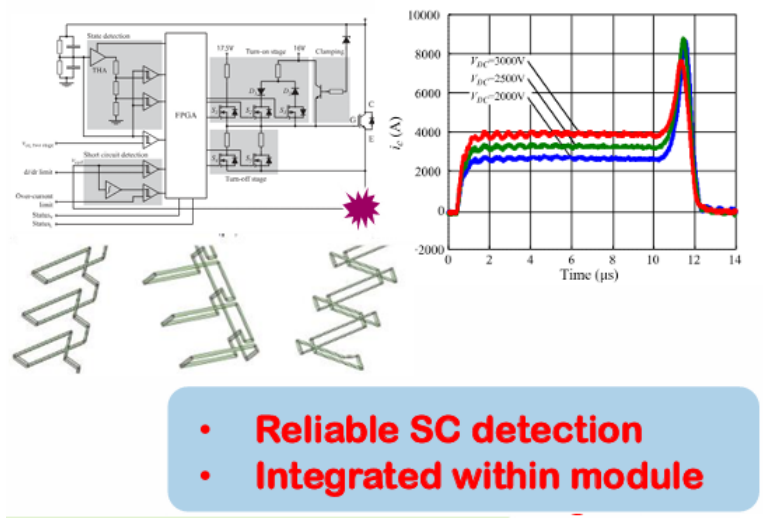

Figure 6: Sensor developed in [20].

In [21], a 180 nm CMOS IC-based isolated hybrid sensor with 3.17 mm^2 die is introduced, combining Hall plates with a differential Rogowski coil for real-time motor control. The Rogowski output is filtered through two fully differential switched-capacitor integrators, enhancing input impedance, CMRR, and limiting bandwidth. The sensor handles an input range of ±4 A, with a slew rate (SR) up to 100 A/μs and a maximum delay of 10 ns.

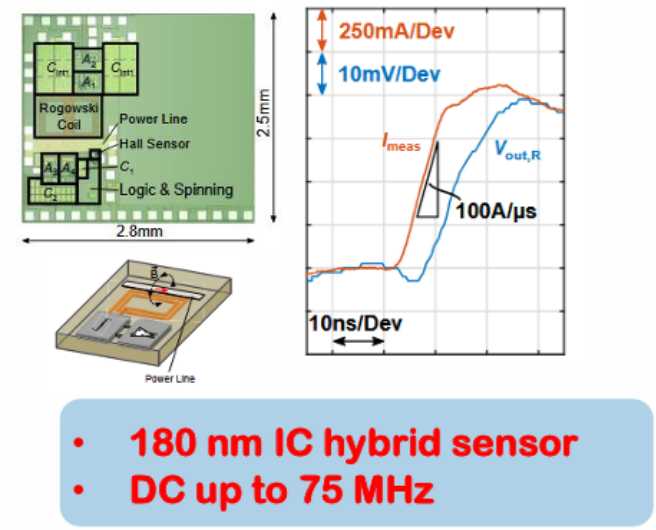

Figure 7: Sensor developed in [21].

In [22], another 180 nm CMOS IC-based hybrid current sensor is proposed, covering DC to 5 MHz with a compact 3.9 mm^2 die. It combines Hall plates with a rectangular spiral coil and includes a DC servo loop to eliminate offset without large blocking capacitors. The architecture minimizes thermal drift and die area, while ripple cancellation suppresses spin Hall-induced magnetic polarization. The prototype accurately tracks ±50 A currents, with an overall gain error of ±2.7%.

2

Rogowski Coils

Executive Summary

This chapter explains the operating principle, modeling and studied topologies. Presents workflow and validation methods. **Main topics covered:**

- Operating principle and lumped model.
- Sensor design workflow and validation for three different realizations.

2.1 Rogowski coils as current sensors

In 1912, W. Rogowski and W.Steinhaus [13] described a coil wound on a flexible nonmagnetic strip for measuring an electric current. This coil was later named the Rogowski coil. Analog measurement had been documented earlier in 1887 by A. P. Chattock [14].

2.1.1 Operating Principle of the Rogowski Coil

The Rogowski coil measures the time derivative of the current flowing through a conductor, utilizing Faraday's law of electromagnetic induction. The induced voltage across the coil terminals, $v_{\text{coil}}(t)$, is directly proportional to the rate of change of the primary current $i_p(t)$, i.e.,

$$v_{\text{coil}}(t) = -M\frac{di_p(t)}{dt} \tag{1}$$

where M is the mutual inductance between the conductor and the coil.

Along a closed path, and according to the Maxwell–Ampère law in the quasi-static approximation:

$$\oint_C \vec{H} \cdot d\vec{l} \approx I_{\text{enclosed}} \tag{2}$$

This relationship forms the basis for current sensing, indicating that the line integral of the magnetic field around a conductor is proportional to the enclosed current.

A time-varying current $i(t)$ in the primary conductor generates a magnetic field $\vec{H}(t)$, which, due to the air core, results in a magnetic flux density:

$$\vec{B}(t) = \mu_0 \vec{H}(t) \tag{3}$$

This flux penetrates the coil turns and induces a voltage according to Faraday's law:

$$\oint_C \vec{E} \cdot d\vec{l} = -\frac{d}{dt} \iint_A \vec{B} \cdot d\vec{A} = -\frac{d\phi}{dt} \tag{4}$$

To recover the primary current waveform $i(t)$, the coil output voltage needs to pass through an integrator circuit.

2.1.2 Lumped Electrical Model and Frequency Response

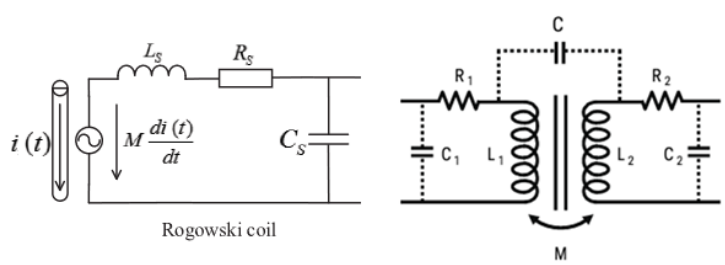

Figure 8: Electrical model of a Rogowski coil

The lumped electrical circuit model of a Rogowski coil -hereinafter also referred to as Pick-Up Coil (PUC)- is equivalent to a transformer when the sensor length is much smaller than the wavelength of the highest frequency component of interest. Considering a two-port model, the primary represents the conductor carrying the current of interest, while the secondary is an adjacent conductor that collects the generated field.

The transfer function of the sensor can be simplified to a derivator when the frequency is much smaller than the first parallel resonance of the secondary winding, determined by L_s and C_s:

$$\boxed{H(s) = sM}.$$

Thus, the frequency response of a Rogowski coil has a zero at the origin. To reconstruct the sensed current, the integrator's cut-off frequency must be at least one decade below the fundamental frequency component of the measured alternating current. This ensures that the overall frequency response gain remains constant and without any phase distortion for frequencies above the imposed low-pass filter limit.

This gain depends on the product of the mutual inductance and the low-pass filter cutoff angular frequency. The first parallel resonance of the secondary winding, determined by L_s and C_s, limits the upper frequency range and dynamic performance of the sensor.

For the sake of simplicity, this transfer function can be derived as the pick-up coil being loaded by a high impedance. Consider a Rogowski coil as depicted in Fig.8 modeled as a series $R_s L_s$ winding with induced voltage $sMI(s)$, and a parallel capacitance C_s.

The voltage on the capacitor follows

$$H_V(s) = \frac{V_{\text{coil}}(s)}{I(s)} = \frac{Ms}{1 + RCs + LCs^2}. \tag{5}$$

From the canonical second order transfer function, the following definitions arise

$$\omega_0 = \frac{1}{\sqrt{LC}}, \tag{6}$$

$$Q = \frac{1}{R}\sqrt{\frac{L}{C}}. \tag{7}$$

As long as the high-Q approximation holds (for $R \to 0$, $Q \gg 1$), the transfer function can be simplified to

$$H_V(s) \approx \frac{Ms}{1 + LCs^2}. \tag{8}$$

Below resonance, $\omega \ll \omega_0$,$LCs^2 \ll 1$. Therefore, the transfer function can be further simplified to

$$H_V(s) \approx Ms. \tag{9}$$

The output voltage of the pick-up coil needs to be integrated in order to reconstruct the sensed current. Given the passive integrator

$$H_{int}(s) = \frac{1}{1 + sR_iC_i}. \tag{10}$$

The total transfer function becomes [2]:

$$H_{\mathrm{t}}(s) = H_V(s) \cdot H_{\mathrm{int}}(s) = \frac{Ms}{1 + sR_iC_i}. \tag{11}$$

Summary

Key considerations for the design of the current sensor:

- **Ensure high-Q approximation**. This holds as long as $Q \gg 1$, $R_s \to 0$ and $Z_{integrator}(s) \to \infty$
- **Ensure the self-resonance frequency of the pick-up coil is much higher than the resonance with the integrator's capacitance** [a]. Therefore, $C_i \gg C_s$.

[a] The resonance with the integrator's capacitance is the real limitation on the bandwidth of the sensor

[2] It needs to be acknowledged that the formula is still same. Nevertheless, conceptually is invalid. It can be easily proved that the pick-up coil loaded by the equivalent input impedance of the passive integrator and working before the self resonance of the coil leads to the same transfer function

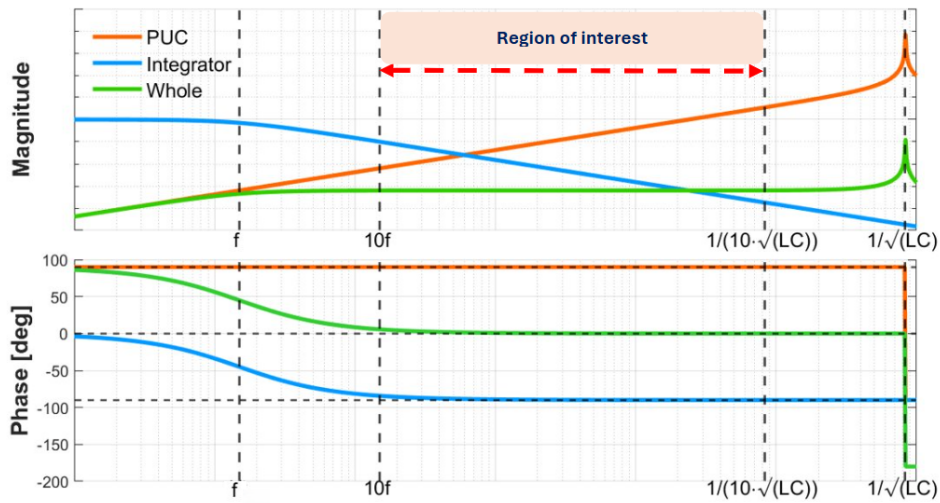

Figure 9: Gain and phase distortion comparison of the frequency response with and without an integrator circuit.

2.2 Researched geometries

Different PCB-integrated PUCs have been reported in the literature. Within this study, three different topologies will be the subject of study.

- **Conventional Rogowski Coil (Coil A)**: The conventional PCB-integrated Rogowski coil geometry directly follows from the helical coil wrapped around a conductor. The main current-carrying conductor is inserted in the center of the PCB.
- **Coplanar Coil (Coil B) [17]**: An increased coupling is achieved with a coplanar arrangement. The coil is embedded between the main conductor, which is wrapped around the PCB.
- **Flat Coil + Flat Conductor (Coil C) [15,16]**: The N turns of the PUC lie equally distributed on both sides of the main conductor (N/2 on each side).

The lack of a systematic approach to cover the design of pick-up coils as current transducers, along with a proper workflow, hinders repeatability and changes in the designs. **This workflow assumes the designed pick-up coil is operated below its first resonance**.

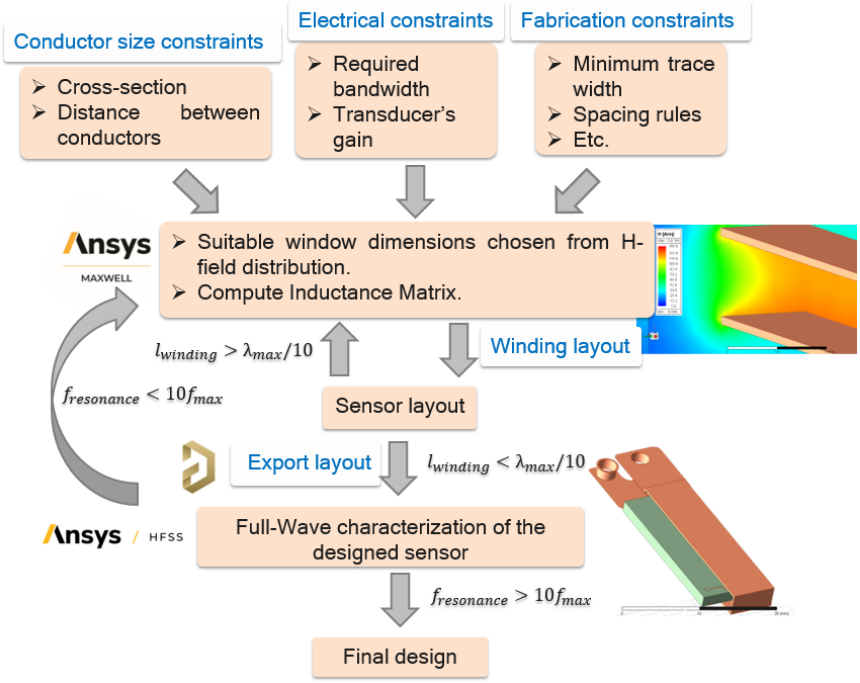

Figure 10: Proposed PUC design workflow.

	Drilling	Traces
1 oz Cu PCB		
Min. hole size (ID)	0.15 mm	–
Min. hole size (OD)	0.25 mm	–
Min. trace width / Min. spacing	–	0.10 / 0.10 mm
Same net min. spacing	–	0.25 mm
Via drill diameter (H)	0.15 mm	–
Via copper diameter (P)	0.25 mm	–

Table 3: JLCPCB Drilling and Trace Capabilities for 1 oz Copper PCBs

On the fabricated PUCs

Since there was not a target sensitivity for the current transducer, the main constraint to which designs were subject was to have a maximum area of $15 \cdot 15\ mm^2$ and to be as compact as the manufacturing process allowed. The height of the embedded windings was set to 1.6 mm. Therefore, **different PUC topologies with similar volumes are compared.**

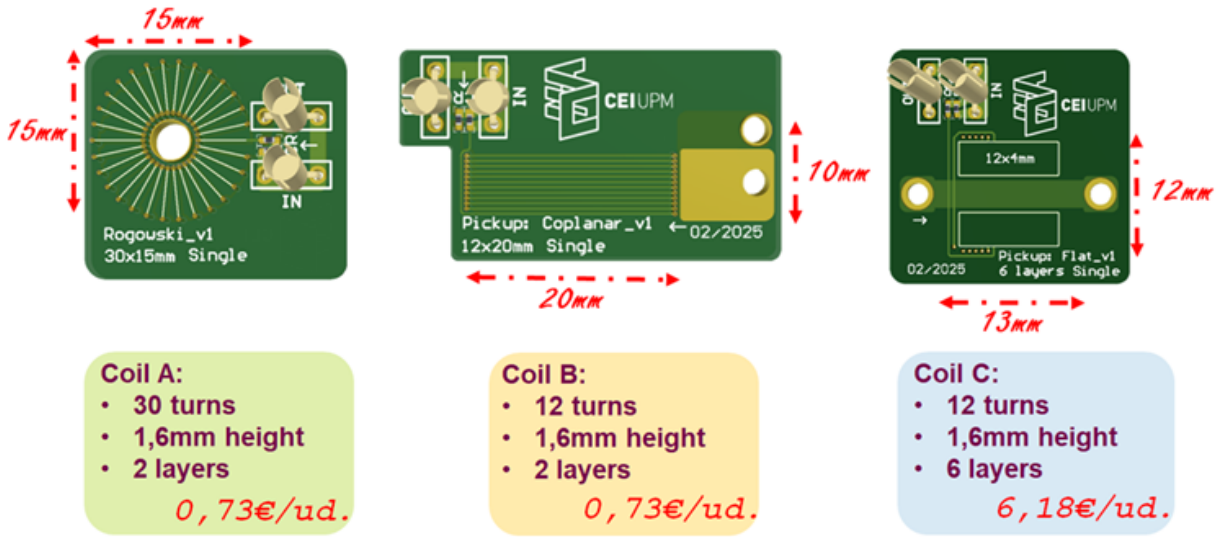

Figure 11: Final designs for each PUC topology.

A remark on the simulations

The quasi-static FEM simulations[a] carried out in *Ansys Maxwell3D* are able to explain magnetic coupling with simplified structures but fail to explain the inductance of very thin conductors (for example, the turns in the flat pick-up coil). Nevertheless, there is good agreement with the results obtained from full-wave FEM simulations in *Ansys HFSS*.

[a] In order to reduce the simulation time, meshing complexity has been simplified through a trade-off between precision and the time spent through each simulation.

2.3 Characterization of the designed PUCs

Several setups and instruments have been used to perform the characterization of the designed PUCs and to cross-validate the results obtained through simulations.

1. **Small signal measurements with E4990A Impedance Analyzer**. This instrument is used to measure the small signal electrical parameters of the PUCs. Is a 50MHz bandwidth impedance analyzer which is able to perform the following measurements: [3]

   (a) L_p. Measured according to the inductance measurement suggestions provided in [23]. The inductance has been determined as the mean value of 5 points taken on the valley of the equivalent inductance[4]. Hence, when the -big- capacitance of the setup [5] and the -small- "self" capacitance can neglected.

   (b) L_s. The same procedure and considerations as before apply to this measurement.

   (c) M. Measured according to the same inductance measurement suggestions. The Fellici balance[6] is a well-know technique to perform this measurement. Nevertheless, if the pick-up coil is model with a T-network, close agreement can be obtained through both methods for **the helical** (A) **and coplanar** (B) **pick-up coil**.

[3] The secondary and primary capacitance need to be measured by the self resonance in the impedance, $|Z|$. Since the bandwidth of the impedance analyzer is well below this resonance, this capacitance could not be determined.

[4] The properties of the involved material don't suggest frequency dependent properties on the low frequency measurement range (up to 50MHz).

[5] The compensation is only able to minimize the influence of the stray parasitics introduced by the acquisition circuit itself, it won't compensate for the additional coupling effects between the DUT and the setup itself.

[6] **Is the only possible way to perform this measurment for the pick-up coil with arrange C**

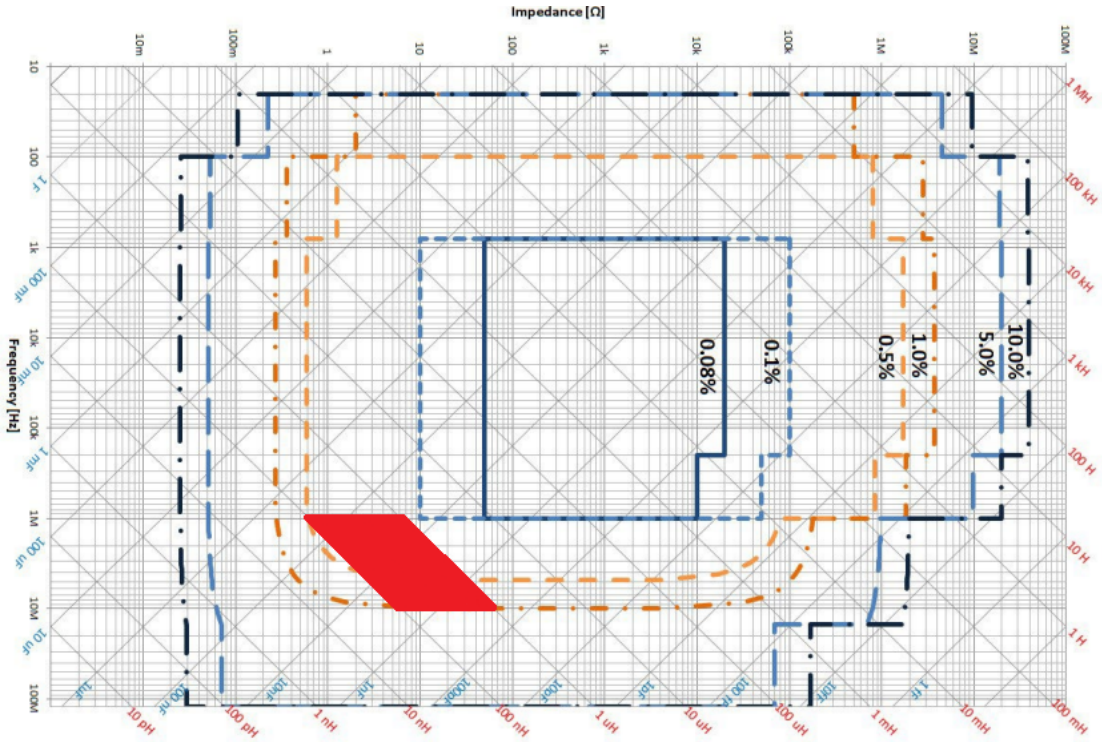

Figure 12: Measurement uncertainty with the E4990A Impedance Analyzer. The area highlighted in red covers the whole range of measurement.

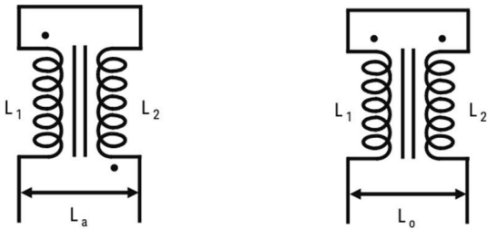

$$L_a = L_1 + L_2 + 2M \qquad L_o = L_1 + L_2 - 2M$$

$$M = \frac{L_o - L_a}{4}$$

Figure 13: Fellici balance measurement principle.

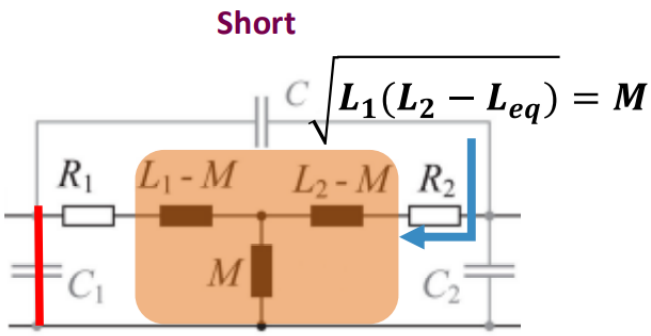

Figure 14: T model measurement principle.

(d) C_{cm}. The inter-winding capacitance is the common mode capacitance for the pick-up coil. In order to avoid the influence of the self-capacitance of the sensed conductor and the winding of the pick-up coil, both the "primary" and "secondary" need to be shorted.

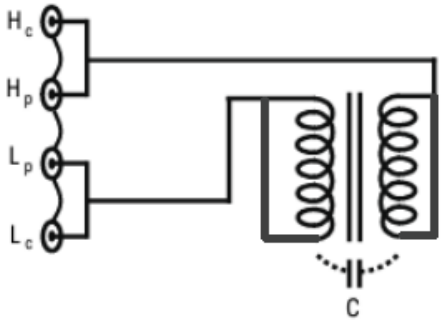

Figure 15: Interwinding capacitance measurement.

On the precision of the measurements

The performed measurements lie in the 1MHz to 10MHz range, the maximum expected error for any of the electrical parameters is less than 5%.

2. **Large signal measurements with Tektronix DPO3014 and RF-Amplifier**. Four-terminal sensing principles are employed with passive and hall-efect current probes in order to measure the same parameters as indicated before. A sinusoidal voltage

(driven by an RF-Amplifier where the oscillation frequency is set by an external signal generator) is applied to the corresponding terminal of the PUC. Phase shift and peak-to-peak amplitudes are translated into the lumped elements of the electrical model of the pick-up coil according to the placement of the excitation and acquisition terminals:

(a) L_p, L_s. Same terminal for excitation and signal acquisition.
(b) M. Opposite terminals for excitation and signal acquisition.

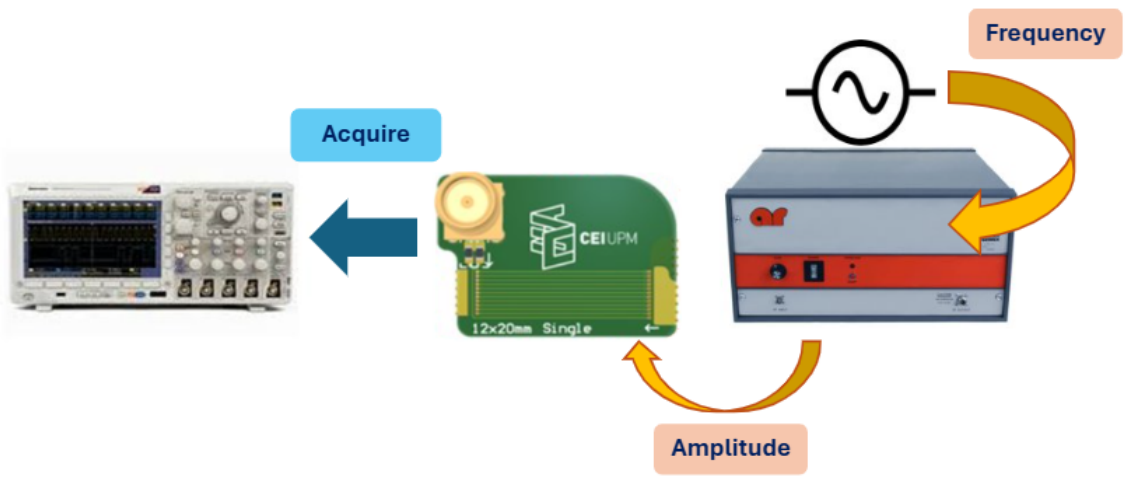

Figure 16: Large signal measurement's setup.

Beware should be taken with these measurements. Several factors hinder their reliability:

(a) **Mutual inductance measurement.** The RF-amplifier is able to deliver up to 3.5 A_{pk}, since the expected mutual inductance is -very- small, the sensed voltage falls to the 1 mV/div range. The oscilloscope when adjusted to this scale has a DC-gain error of 2.5% and which is expected to hold constant for the low frequency range.
(b) **Deskew between channels**. According to the datasheet, the maximum deskew that can be performed between channels is ± 100 ns. Through a resistor calibration over the mea-

surement frequency range ($150kHz - 1MHz$) a mean $\pm 5\ ns$ (1σ) skew has been observed.

Let:

$$y(x) = \cos\big(2\pi f x\big), \text{ with uncertainty } \Delta x$$

Applying first–order uncertainty propagation,

$$\Delta y \;\approx\; \left|\frac{dy}{dx}\right| \Delta x \;=\; 2\pi f \left|\sin\big(2\pi f x\big)\right| \Delta x.$$

Thus, the relative uncertainty in y:

$$\frac{\Delta y}{|y|} \;\approx\; \frac{2\pi f\,|\sin(2\pi f x)|\,\Delta x}{|\cos(2\pi f x)|} \;=\; 2\pi f\,\Delta x\,\big|\tan(2\pi f x)\big|.$$

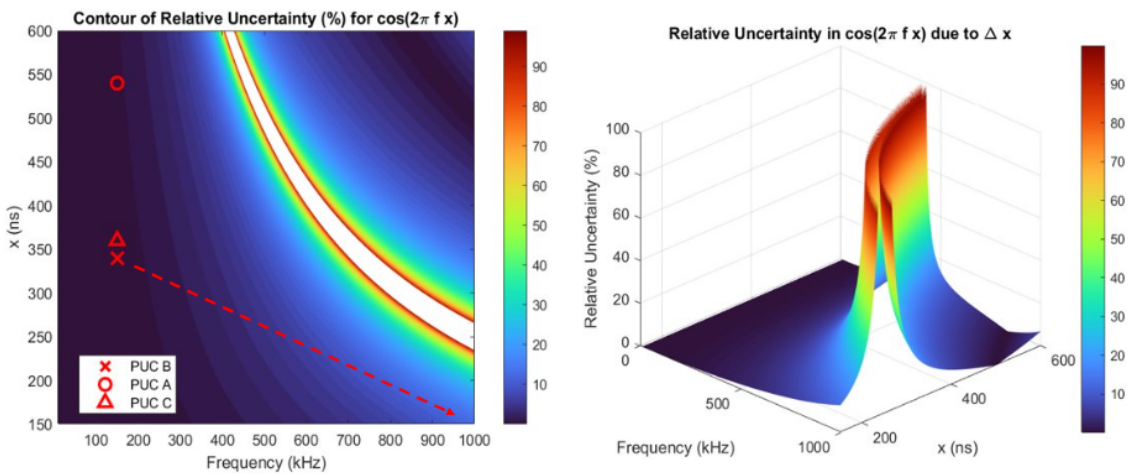

Figure 17: 3σ uncertainty for real term.

The same holds true for the "imaginary" term, therefore:

$$\frac{\Delta y}{|y|} \;\approx\; \frac{2\pi f\,|\cos(2\pi f x)|\,\Delta x}{|\sin(2\pi f x)|} \;=\; 2\pi f\,\Delta x\,\big|\cot(2\pi f x)\big|.$$

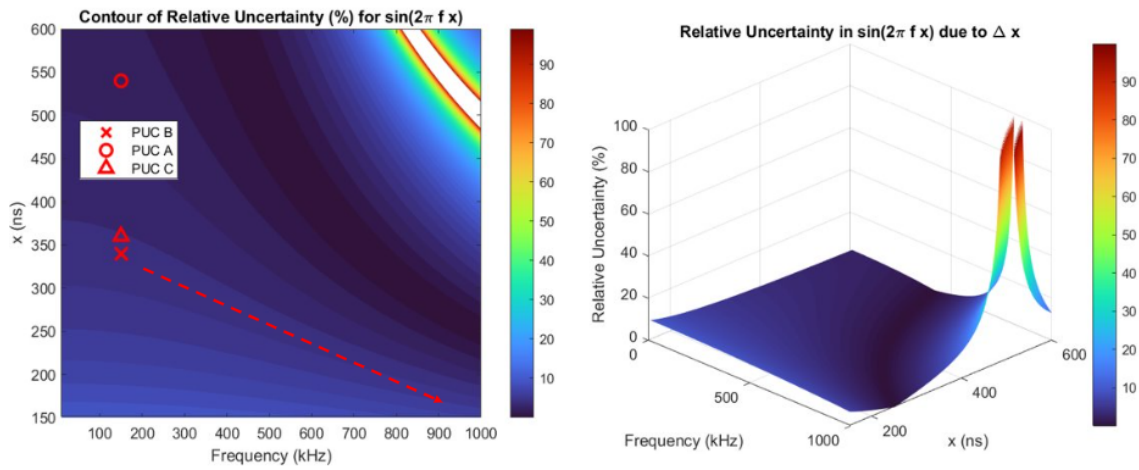

Figure 18: 3σ uncertainty for imaginary term.

On the large signal measurements

- From the relative uncertainty analysis at (3σ) the measures at $150kHz$ are the ones which explain the energy distribution within the pick-up coils with less uncertainty.
- Differences from large and small signal measurements arise from the uncertainty of the measurement itself. The large signal behavior is expected to be the same as the small signal since the properties of the involved materials (copper, FR4 and air) are stable within room temperature, low-voltages and below-GHz frequencies.

2.3.1 On the PUC's winding resistance

Thorough analysis of the winding resistance through simulation requires specific surface meshing and general extensive meshing in order to increase the precision of the simulations' results. For example, results for the classical helical topology (PUC A) with standard meshing are depicted in fig. 19.

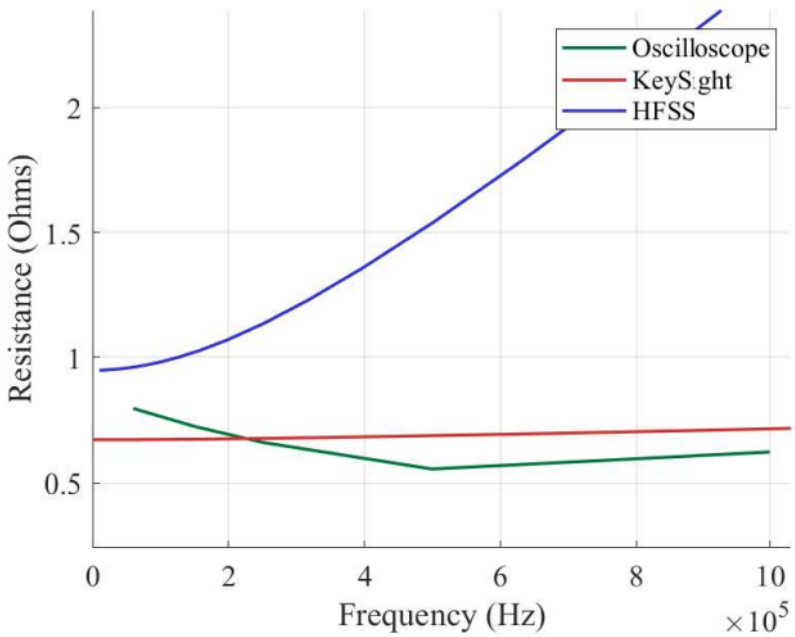

Figure 19: Comparison between $R_{seconcdary}$ measurements for PUC A.

It has been experimentally checked that the **resistance values for every arrangement satisfy the high-Q approximation**, essential for the sensor's design.

2.4 Results

Once discussed the tools, the design procedure and the measurement methods with practical takeaways, the key results and arrangement selection will be covered. Table. 4 shows the main electrical parameters of the designed PUCs, along with the comparison between simulation results and experimental measurements. In Table. 5 the different designs are qualitatively compared.

	Maxwell3D	HFSS	Small Signal	Large Signal @150kHz
		Coplanar		
L_p (nH)	14.259	9.20	14.389	11.048
L_s (nH)	959.29	719.16	743.72	799.16
M (nH)	48.236	45.385	42.20	43.789
$k6^0$	0.412	0.558	0.408	0.470
C_{12} (pF)	–	11.09	14.148	–
SRF (MHz)	–	128.68	–	–
		Flat7^0		
L_p (nH)	11.648	10.59	11.289	12.42
L_s (nH)	1918.4	934.79	987.62	849.84
M (nH)	25.46	20.00	22.545	21.43
k	0.170	0.200	0.210	0.210
C_{12} (pF)	–	6.07	4.98	–
SRF (MHz)	–	158.49	–	–
		Rogowski		
L_p (nH)	5.66	27.18	24.257	29.34
L_s (nH)	435.96	361.49	341.32	429.50
M (nH)	11.932	12.17	13.169	13.38
k	0.242	0.123	0.160	0.120
C_{12} (pF)	–	2.077	1.825	–
SRF (MHz)	–	316.22	–	–

Table 4: Comparison of extracted parameters for Coplanar, Flat, and Rogowski structures at 150 kHz.

$6^0k = \frac{M}{\sqrt{L_pL_s}}$ 7^0An homogenization of the sensed conductor with Dowell method was used in order to perform the simulation in Maxwell3D.

Metric	Best	Medium	Worst
Coupling k	Coplanar (0.408)	Flat (0.210)	Rogowski (0.160)
M (nH)	Coplanar (42.20)	Flat (22.55)	Rogowski (13.17)
L_p (nH)	Flat (11.29)	Coplanar (14.39)	Rogowski (24.26)
L_s (nH)	Rogowski (341.3)	Coplanar (743.7)	Flat (987.6)
C_{12} (pF)	Rogowski (1.83)	Flat (4.98)	Coplanar (14.15)
SRF (MHz)	Rogowski (316.2)	Flat (158.5)	Coplanar (128.7)

Table 5: Qualitative ranking of geometries (small-signal parameters, SRF from HFSS).

Selected arrangement

The coplanar arrange (PUC B) has the best mutual inductance for similar total volume. It is among the least expensive arrangements. The coplanar arrangement magnetically couples "forth and back" sensed conductors, which decreases the inductance introduced by the sensor. Although the SRF is the worst from all the possible arrangements (which hints a greater secondary capacitance than the flat arrangement), the maximum expected bandwidth ($12.8MHz$) is enough for most power converters (unless very-high frequency VRMs). An additional consideration must be taken due to the interwinding capacitance; **to fully leverage the PUC, the sensor must be placed at a quiet-voltage node**.

3

Sensor Realization

Executive Summary

This chapter addresses the sensor manufacturing process and characterization. Assesses the impact within the power loop. **Main topics covered:**

- Manufacture of PCB prototypes and sensitivity characterization.
- Analysis of loop impedance impact.

3.1 Main constraints of the designed sensor

As already discussed in the previous chapter, in order to sense the current effectively, it is necessary to integrate the output voltage at the terminals of the coil. The sensor was designed in order to track an **arbitrary current with its main harmonic at** $150kHz$.

Parameter	Value
$R_{integrator}$	$100k\Omega$
$C_{integrator}$	100pF
$G_{expected}$	$4.22\frac{mV}{A}$

Table 6: Parameters of the manufactured sensor.

3.2 Gain measurement

Large signal measurements have already been discussed in the previous chapter. In order to perform the small signal gain measurement, a **Bode100**, along with an RF-amplifier to drive the PUC, is used to

calculate the transmission coefficient between both input ports of the instrument. The setup for this measurement is depicted in Fig. 20.

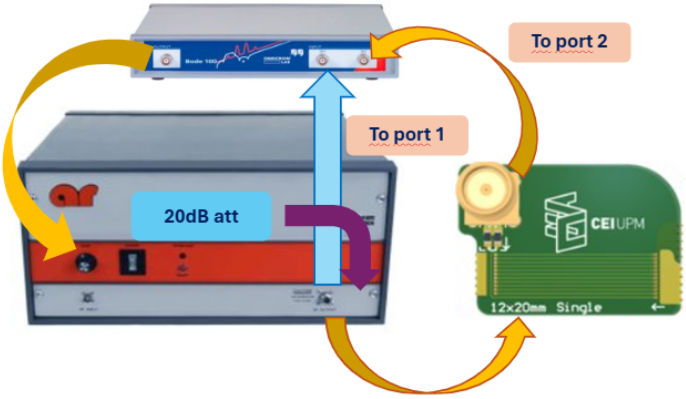

Figure 20: Small-signal sensitivity measurement.

On the uncertainty of gain measurement

- **Small signal thru calibration can't be performed with the amplifier in the loop.** The only way to perform this measurement is to de-embed the DUT's transmission parameters by removing the amplifier's transmission matrix (along with the rest of the connectors) to the whole setup. **Experimental results show a -nearly systematic- error of $-1dB$ compared to the theoretical expected value, and -arguably- explained as the shift in the reference plane introduced by the coaxial connectors.** Nevertheless, beware needs to be taken with this given setup.
- The large signal measurement accounts for the same discussed uncertainty of the lumped element characterization of the pick-up coil.

Additional considerations regarding the internal configuration of the **Bode100** are shown in the following table:

Parameter	Channel 1 / Receiver 1	Channel 2 / Receiver 2
Receiver bandwidth	100 Hz	
Source level	6 dBm	
DUT settling time	0 s	
Sweep time	5.61 s	
Termination	50 Ω	1 MΩ
Gain	50 Ω	1 MΩ
Impedance	50 Ω	1 MΩ
Receiver switch	Receiver 1	Receiver 2
Transmission/Gain	External	External
Impedance/Reflection	Internal	Internal
Attenuator setting (T/G)	20 dB	0 dB
Attenuator setting (I/R)	10 dB	10 dB

Table 7: Hardware configuration and measurement setup.

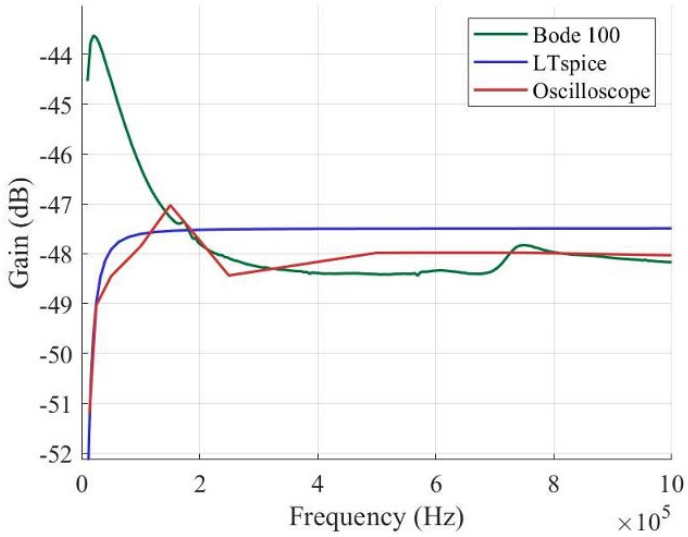

Figure 21: Sensitivity comparison for the first designed sensor.

3.3 Designed sensor

In order to ease the soldering of the sensed conductor in the coplanar arrangement and to ensure minimal and uniform separation, instead of "wrapping" a single conductor around the winding, castellated copper vias are placed within the coil's winding PCB.

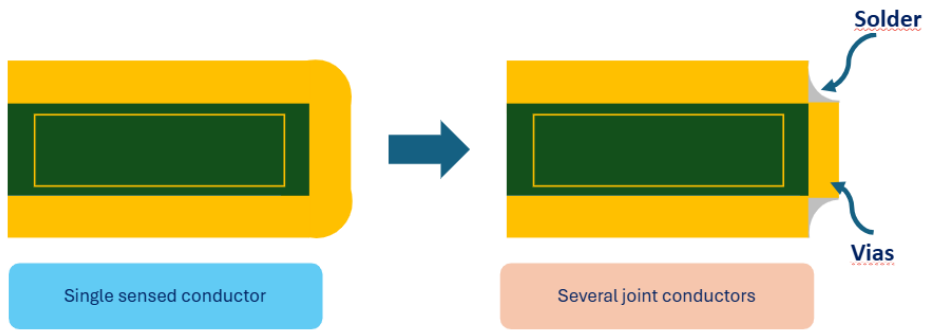

Figure 22: Suggested layout modification for the sensed conductor.

Parameter	Value
R	$100k\Omega$
C	100pF
M	46nH
$G_{expected}$	$4.6\ \frac{mV}{A}$
$G_{small-signal}$	$4.537\ \frac{mV}{A}$

Table 8: Main parameters of the designed sensor

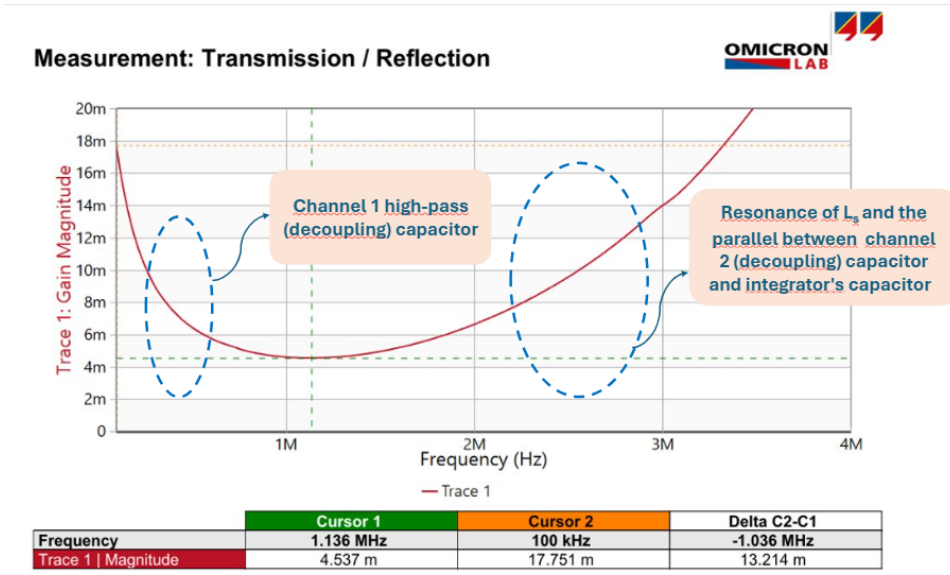

Figure 23: Small-signal measurement of the designed sensor.

3.4 Discussion on the impedance inserted into the power loop

The impedance of the integrator at the secondary follows

$$Z_L = R + \frac{1}{j\omega C}.$$

As long as the pick-up coil behaves as a two-terminal transformer, the reflected impedance at the primary is

$$Z_{\text{reflected}} = -\frac{(\omega M)^2}{Z_L + j\omega L_2} = -\frac{(\omega M)^2}{R + j\left(\omega L_2 - \frac{1}{\omega C}\right)}.$$

In real and imaginary parts:

$$Z_{\text{reflected}} = -\frac{(\omega M)^2 R}{R^2 + X_2^2} + j\frac{(\omega M)^2 X_2}{R^2 + X_2^2}, \quad X_2 = \omega L_2 - \frac{1}{\omega C}.$$

From the equation above, it is clear that

- Large R increases the resistive component of the reflection

- Small R makes the reflected term more "reactive".

At low frequencies, the resistive term dominates. At high frequencies, the reactive part dominates due to $X_2 \approx \omega L_2$.

Regarding the capacitance,

- At low frequencies, $1/(\omega C)$ dominates, making X_2 negative. Therefore, the reflected impedance is slightly capacitive.
- At high frequencies, ωL_2 dominates, and the reflection becomes inductive.

Since $(\omega M)^2 = (\omega k\sqrt{L_1 L_2})^2$, the following can be inferred:

- Stronger coupling (larger k) or higher mutual inductance increases the magnitude of the reflected impedance.
- Weak coupling or small M reduces the reflected impedance, making the intrinsic primary impedance dominant.

Including the primary resistance R_p and inductance L_1, the total impedance seen at the primary is:

$$Z_{\text{total}} = Z_p + Z_{\text{reflected}} = R_p + j\omega L_1 - \frac{(\omega M)^2}{R + j\left(\omega L_2 - \frac{1}{\omega C}\right)}.$$

The primary impedance Z_p dominates at low and high frequencies if R is large or M is small [7].

- The reflected impedance introduces frequency-dependent behavior in the primary, with a mostly inductive character at higher frequencies and a possible capacitive effect at low frequencies.
- Load resistance R controls the real part of the reflection, while capacitance C controls the transition between capacitive and inductive behavior.

[7] Near the resonant frequency of the secondary LC, the reflected term has a noticeable effect.

- Coupling coefficient k and mutual inductance M scale the magnitude of the reflected term.
- The total primary impedance is the sum of the primary and reflected impedances, and its accurate evaluation is critical for transformer design and signal integrity.

On the reflected impedance

- The reflected impedance is small compared to the primary impedance, due to the large load impedance and weak coupling.
- The phase of the reflected impedance is mostly inductive across the frequency range from 15kHz to 1MHz.
- The total primary impedance is dominated by the primary winding, the secondary reflection is negligible.

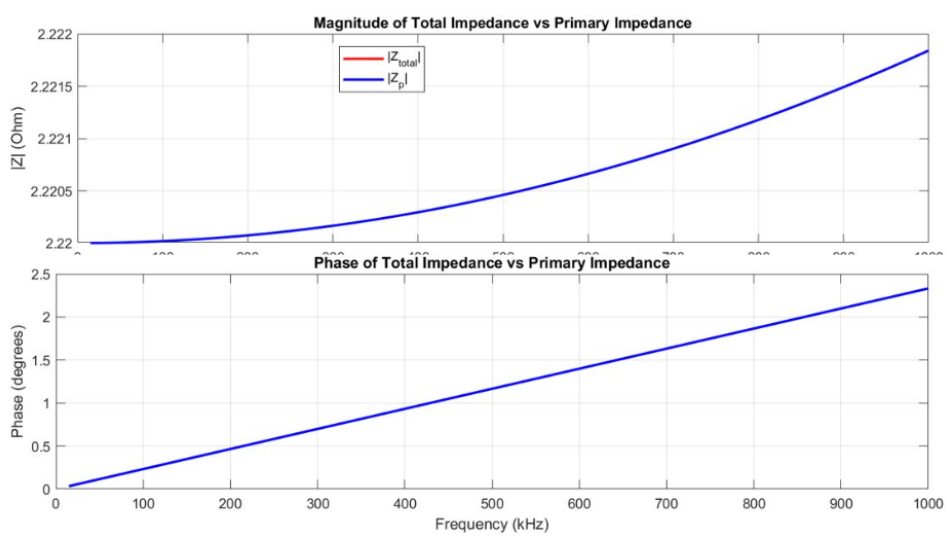

Figure 24: Total reflected impedance compared to the primary impedance.

4

Experimental Validation

Executive Summary

This chapter evaluates the performance of the designed sensor in two power converters with WBG devices. It assesses behavior under realistic operation. **Main topics covered:**

- Integration of the designed sensors.
- Analysis of sensor behavior in real conditions.

4.1 Researched converter topologies for PUC validation

The main aim of this MSc thesis is to assess the feasibility of embedded pick-up coils in WBG DC-DC converters. Nevertheless, certain DC-DC converter topologies (controlled in a specific way) are well suited to perform power factor correction from the grid. Therefore, to evaluate the performance of the sensor, two different well-known power converter prototypes with WBG devices are designed [8]:

- **GaN Synchronous CCM Buck.** A classic DC-DC topology which reduces the input voltage.
- **SiC CrCM PFC Boost.** A well-known PFC topology which increases the average rectified grid voltage while draws "in-phase" current.

In both converters, the purpose of the sensor is to measure the ripple current through the inductor. Hence, the sensor needs to be placed at a quiet potential node to avoid interference from high dv/dt (coupled

[8] The design of both topologies **is not covered**

through common mode capacitances). Thus, to avoid - if possible - placing the sensor on the switching node.

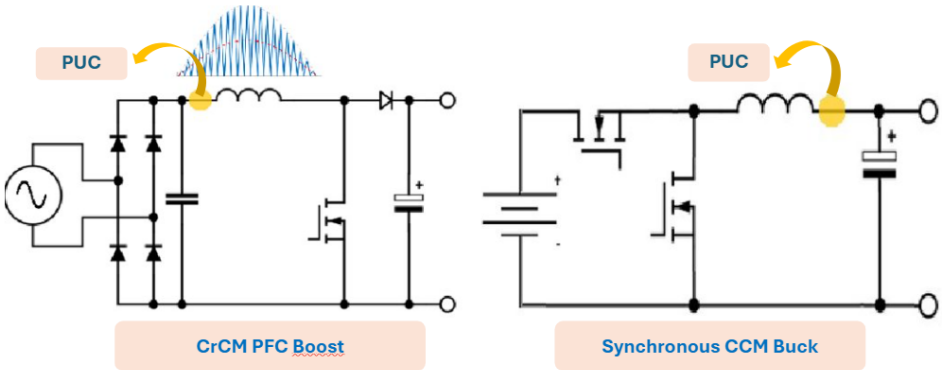

Figure 25: An example image.

Remark on the placement of the sensor

To ease the sensor's signal acquisition and manipulation within the prototype, the sensor has been placed as depicted in Fig. 28. Nevertheless, the optimal layout is achieved if the sensor is placed in the reference/common terminals. This is true even if the inductor is split into both positive and negative terminals (this impedance sharing avoids "moving" common-mode voltage into differential-mode).

4.1.1 SiC PFC Boost converter

The boost power factor correction (PFC) converter is widely adopted in AC–DC conversion stage to shape the grid current. The main function is to shape the input current such that it follows the rectified line voltage, aiming to achieve a unity power factor.

When operated in Critical Conduction Mode (CrCM), the inductor is completely de-energized at the end of every switching cycle. As a result, the converter operates at the boundary between continuous and discontinuous conduction. The inductor current exhibits a triangular waveform, beginning and ending at zero in each cycle, whose mean value across half a grid cycle is a sinusoidal current on-phase with the line voltage.

A key characteristic[9] of CrCM operation is the variable switching frequency, which decreases near the peak of the input voltage and increases towards the zero crossings. CrCM boost PFC converters are usually found in low-power consumer applications, achieving a balance between simplicity and efficiency.

Boost Converter Parameters	
P_{out} (W)	35
η (%)	90
f_{sw} (kHz)	[52.25-100.4]
V_{in} (V_{rms})	56
V_{out} (V)	160
pf	0.9875

Table 9: PFC Boost converter parameters.

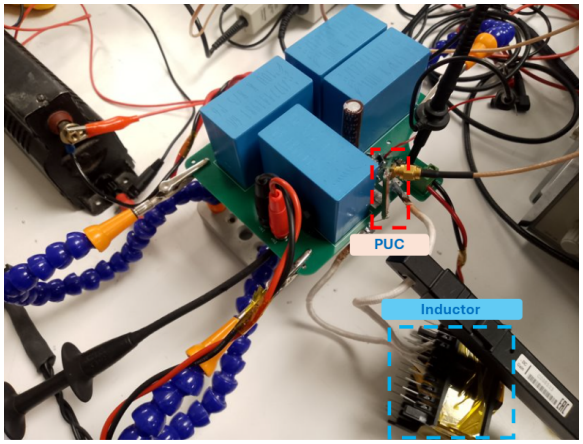

Figure 26: SiC PFC Boost converter prototype.

In Table.10 the measured sensitivity at the peak and valley of the rectified voltage is compared to the nominal value [10].

[9] Besides input current control loop can be neglected. Since the inductor has energy at the end of every cycle, the current through the inductor at every switching cycle can be controlled as "resistive-like" behavior

[10] The current-probe is limited to 50MHz while the PUC channel is limited to 20MHz. This applies for the GaN buck converter as well

Boost Converter Gain $\frac{mV}{A}$	
Gain @ $f_{\text{sw,max}}$	4.73
Gain @ $f_{\text{sw,min}}$	4.5
Nominal sensitivity (single-frequency)	4.6

Table 10: Measured gain comparison.

Key considerations for the PUC in the PFC converter

- Operation below the region of interest results in amplitude and phase distortion of the low-frequency harmonics. Nevertheless, this effect does not propagate to the detection of rising and falling edges, since a significant number of high-frequency harmonics are "injected" in that region, making the overall instantaneous signal phase shift negligible.
- The asymptotic behavior of the gain in the vicinity of $10f_{integrator}$ accounts for the fact that the sensor sensitivity remains close to its nominal value, even when operating below the nominal frequency
- The presence of additional harmonics must be considered, as they contribute to an increase in the nominal gain (which has been experimentally measured through single-tone) as can be verified from the behavior near the rectified voltage zero crossings. Nevertheless, the Fourier decomposition of this signal reveals that the majority of its power is concentrated in the lower-order harmonics. Consequently, the measured gain remains close to the expected nominal value, as most of the power is in the fundamental harmonic, corresponding to the switching frequency at that point in the grid cycle.

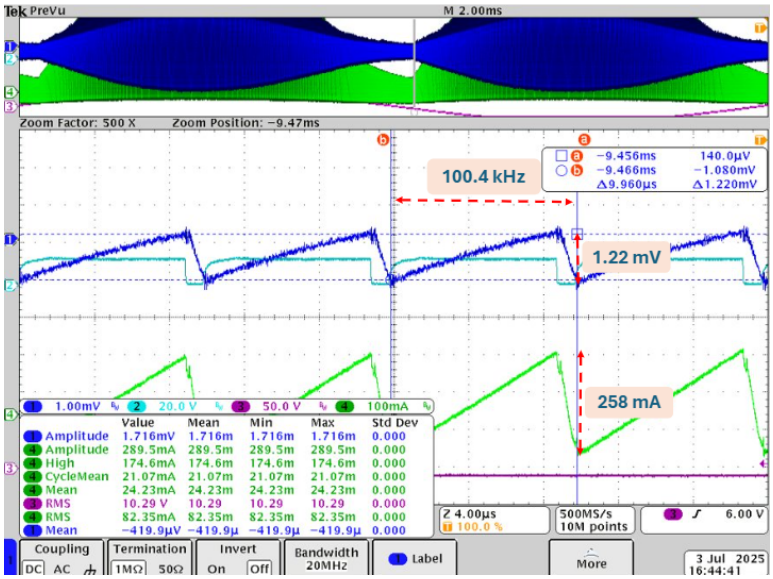

Figure 27: Current sensed with current-probe and sensed with PUC at $100kHz$.

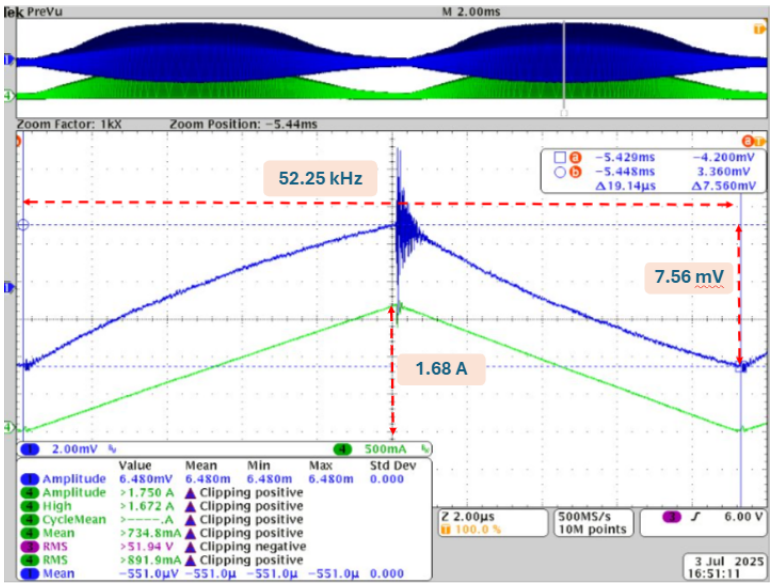

Figure 28: Current sensed with current-probe and sensed with PUC at $52kHz$.

4.1.2 GaN Buck converter

The synchronous buck converter is a fundamental step-down topology widely employed in DC–DC conversion. It reduces an input voltage to a lower output voltage. During each switching cycle, energy is stored in the inductor's magnetic field and then released to the load, while the output capacitor smooths the resulting voltage by acting as an energy buffer. In the synchronous configuration, the diode is replaced by an actively controlled switch.

When operating in Continuous Conduction Mode (CCM), there is still energy stored in the inductor at the end of each switching cycle. Therefore, the inductor current never reaches zero. In this operation mode, the current oscillates around its average value with a triangular ripple.

Buck Converter Parameters	
P_{out} (W)	[5, 100]
f_{sw} (kHz)	[199kHz]
V_{in} (V)	[10, 50]
G (V/V)	0.5

Table 11: Buck converter parameters.

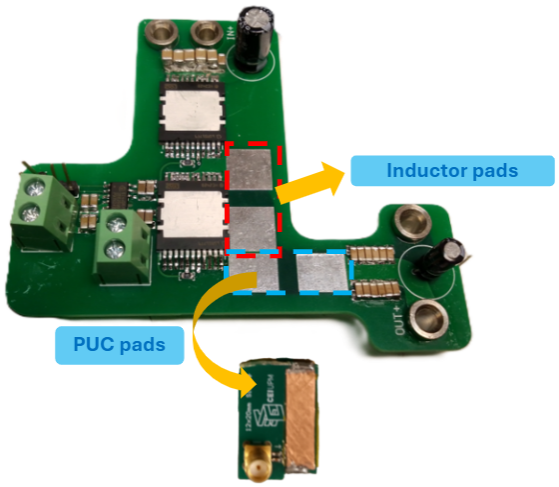

Figure 29: GaN Buck converter prototype.

In Table.12 the measured sensitivity at the maximum and minimum power ratings is compared to the nominal value.

Boost Converter Gain $\frac{mV}{A}$	
Gain @ $P_{\max}$	4.730
Gain @ $P_{\min}$	4.76
Nominal sensitivity (single-frequency)	4.6

Table 12: Measured gain comparison.

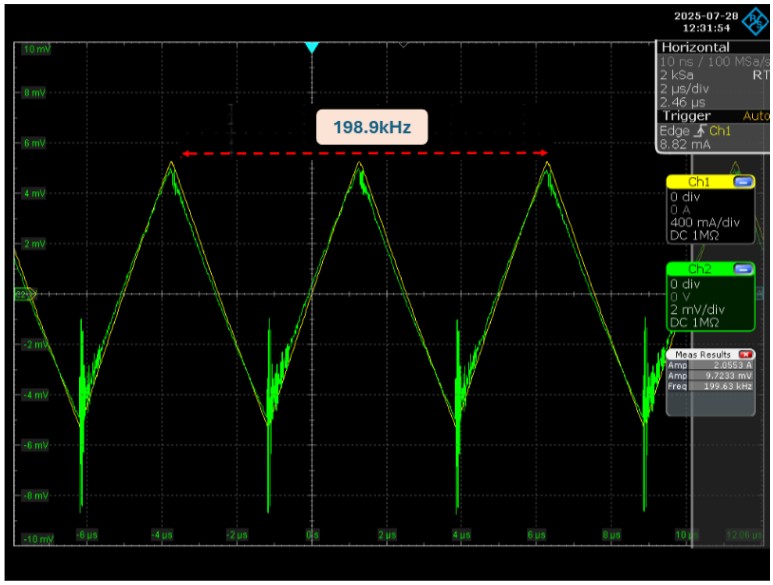

Figure 30: Current sensed with current-probe and sensed with PUC at $100W$.

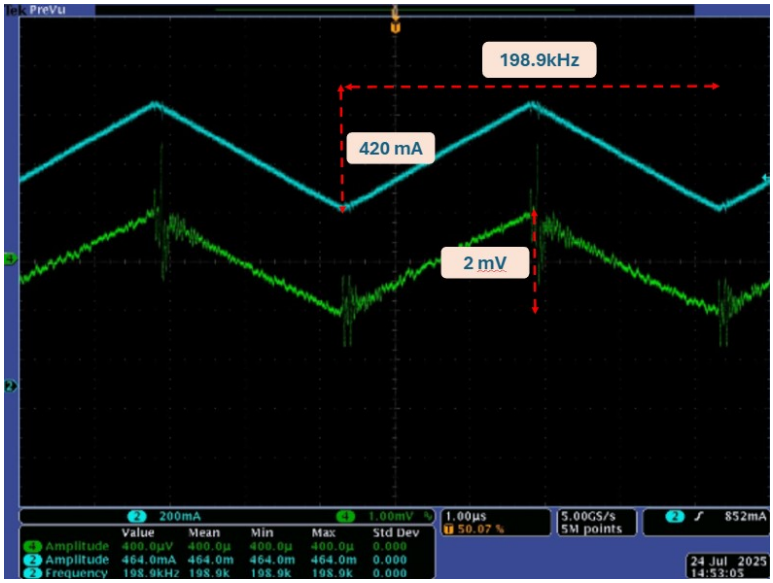

Figure 31: Current sensed with current-probe and sensed with PUC at $5W$.

Key considerations for the PUC in the Buck converter

- Since the fundamental frequency is above $10f_{integrator}$ there is no phase-distortion on the acquired signal by the PUC sensor.
- The presence of additional harmonics must be considered, as they contribute to an increase in the nominal gain as was already mentioned in the previous section. Nevertheless, since the nominal gain is ensured for every harmonic component of the acquired signal, the overall gain is greater than the nominal value.

4.1.3 Comment on the nature of the ringing

Regardless of the converter topology, high-frequency ringing can be appreciated on every "edge". This resonant oscillation happens, as already mentioned in the previous chapter, due to power amplification of the harmonic content in the vicinity of the resonance between the

integrator's capacitor and the PUC's winding inductance [11].

Summary of integrator circuit constraints

It is advisable that the designed integrator complies with:

- $R_{integrator} \rightarrow \infty$
- $C_{integrator} \rightarrow 0$
- $C_{integrator} \gg C_s$.

This ringing can be misunderstood as:

- the modulation -direct- effect of the driving signal on the drawn current from the voltage source.
- the presence of common-mode noise.

This ringing takes place due to the non-linear switching behavior of the devices. It is the current evolution itself within the power converter that sets the overall dynamic response of the acquired signal. Therefore, soft-switching techniques, which intrinsically filter high frequency content from step-like behavior in the state-variables of the circuit, are able to minimize the oscillations.

On the delay of the gate control

The gate driving signal has the same frequency components regardless of the time delay between both sides of the half-bridge. Hence, if the low-side switch is allowed to turn on under ZVS conditions, the current in the power loop won't change abruptly. Therefore, the power of the harmonic content in the vicinity of the aforementioned resonance is reduced.

[11] To correctly visualize the harmonic content of the signal at the edges, FFT ought to be performed

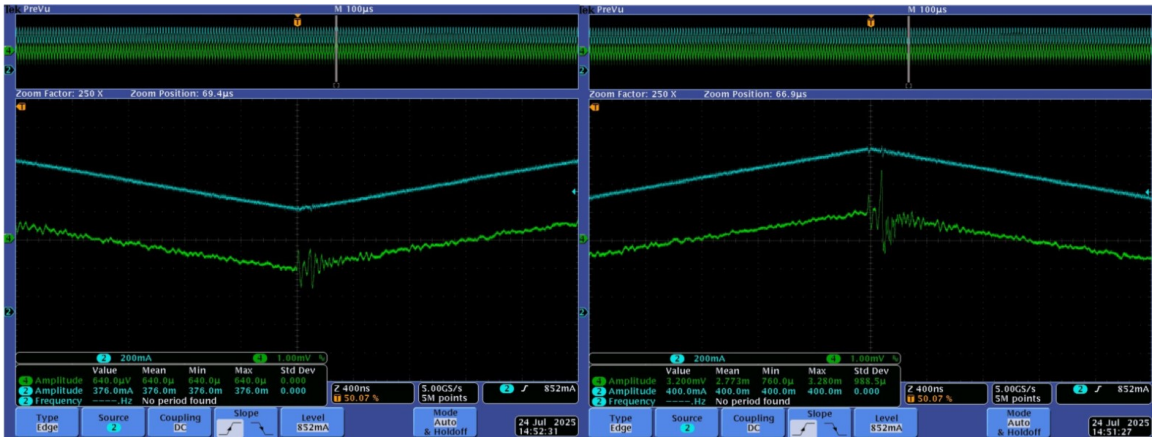

Figure 32: Current sensed with current-probe and sensed with PUC with 20 ns dead-time in the Buck converter.

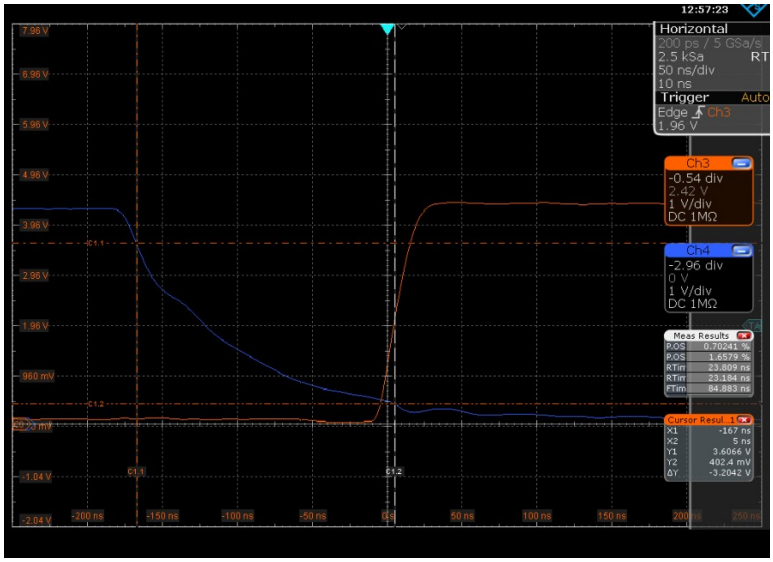

Figure 33: high-side gate control and low-side gate control. The 20 ns dead-time is not enough for low-side switch to achieve ZVS [12].

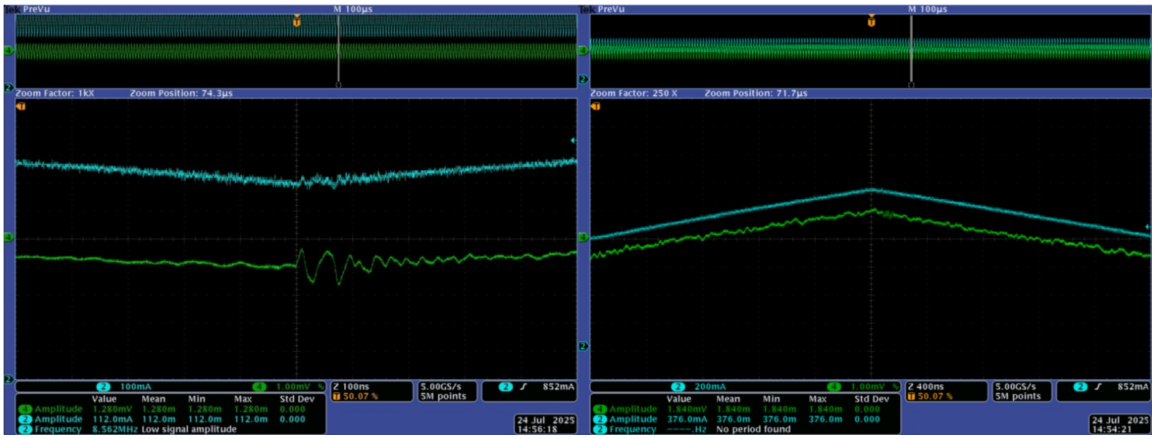

Figure 34: Current sensed with current-probe and sensed with PUC with 60 ns dead-time in the Buck converter.

On the damping of the gate control

It is interesting to note that over-damping the step response of the gate driver avoids abrupt transitions within the power loop. Although the -big- internal gate resistance of SiC devices eases the damping control (hindering fast-switching), for GIT GaN, the fundamental trade-off between dissipated power and the damping is even more critical (a slower response comes at the cost of increased power loss due to the current required to ensure the HEMT is turned on).

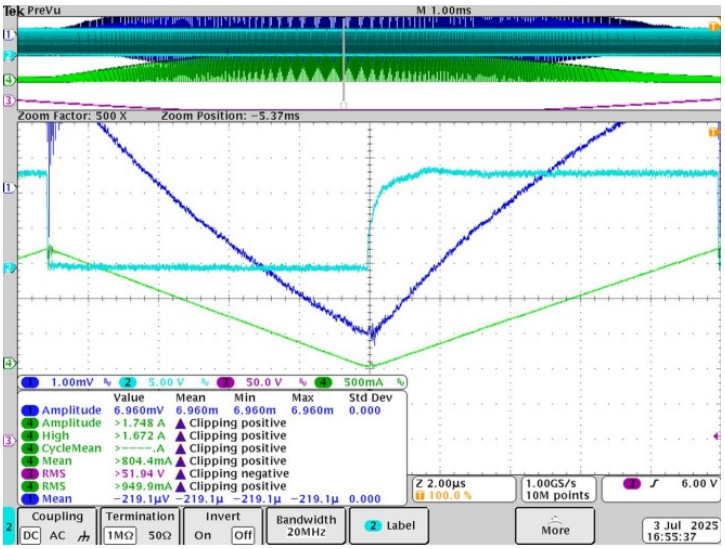

Figure 35: Current sensed with current-probe and sensed with PUC in the low-side turn-on of the PFC Boost converter.

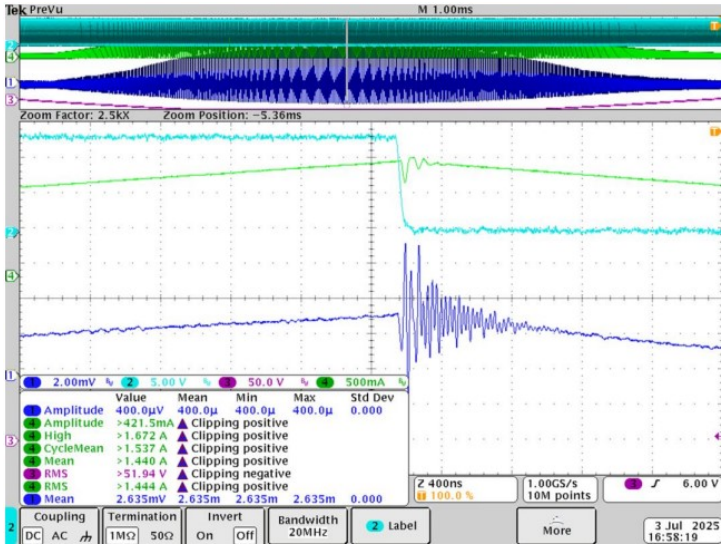

Figure 36: Current sensed with current-probe and sensed with PUC in the low-side turn-off of the PFC Boost converter.

5

Figures of Merit & Design Guidelines

Executive Summary

In this chapter, several FoM to compare PUC topologies and design guidelines are discussed. **Main topics covered:**

- FoMs for sensitivity, bandwidth and form factor.
- Practical guidelines for the design of PUC B coil (coplanar arrangement).

5.1 Motivation

The overall purpose of this chapter is to address the most general constraints on the design of coplanar pick-up coils, which allows further optimization. First, several Figures of Merit (FoM) are proposed to ease the comparison between designs of pick-up coils regardless of the geometry being implemented. Later, general design workflow for pick-up coils as current transducers will be revisited. Finally, design constraints and guidelines for coplanar pick-up coils will be assessed.

5.2 Proposed metrics to compare pick-up coils

In the reviewed literature, -usually- reported parameters are the mutual inductance M and the total covered area of the whole sensor. Furthermore, the magnetic coupling k is overlooked. In the worst cases, no explicit references to the key parameter in these sensors, the mutual inductance M, is even acknowledged. Nevertheless, M alone is an unreliable measurement for the sake of comparing different designs. Therefore, the mutual inductance is given along with the area covered. The different topologies at which the pick-up coils can be presented make the total covered area an unsuitable -standalone- measurement.

Hence, the nature of the metrics should aim to basic engineering practical knowledge. They ought to rely on the working principles regardless of how this solution has been implemented. **The suggested metrics intrinsically promote compact designs**. Four different FoM are suggested:

- η_M. Is the **mutual inductance surface density per turn**. Simplified relationships for Ampère's Law and Faraday's Law [13] (within an isotropic medium and homogeneous field) constitute the magnetic analysis of the pick-up coils. The following system of equations arises

$$\begin{cases} Hl_m = I \\ v = N\frac{d\Phi}{dt} \\ \Phi = \int_A B\,dA \approx BA \\ B = \mu H \end{cases} \tag{12}$$

  where A is the area covered by a turn of the pick-up coil, Φ stands for the magnetic flux, N for the number of turns, I for the sensed current and l_m for the mean magnetic path.

  Solving the system given by sys.12, a relationship between the time derivative of the sensed current and the induced voltage can be derived as

$$v = \underbrace{\frac{NA\mu}{l_m}}_{M=AN\eta_M} \frac{dI}{dt}$$

  Hence η_M is defined as

$$\boxed{\eta_M = \frac{\mu}{l_m} = \frac{M}{AN}\ in\ (H/m^2 turn)} \tag{13}$$

- G_{max}. Is the **maximum attainable gain**. As already discussed in previous chapter, the inherent small signal pick-up coil dynamic

[13] Given the usual sign convention in magnetic components design

response below first series resonance (ω_{res}) can be approximated by a high pass filter. In order to reconstruct the signal an integrator needs to be added whose cut-off frequency needs to be at least a decade before the first resonance (for the shake of model validity). Hence the maximum attainable gain corresponds to

$$\boxed{G_{max} = 2\pi M \frac{f_{res}}{10} = M \frac{\omega_{res}}{10} \quad in\ (V/A)} \tag{14}$$

- $\eta_{G_{max}}$.Is the **maximum attainable gain density per turn**. This metric aims to relate the two previous metrics, as it is derived from the eq.14 in terms of η_M. Therefore:

$$\boxed{G_{max} = \underbrace{M}_{AN\eta_M} \frac{\omega_{res}}{10};\ \eta_{G_{max}} = \eta_M \frac{\omega_{res}}{10} \quad in\ (\frac{V}{Am^2 turn})} \tag{15}$$

- κ. Most designs found in literature lack to explicitly report the total volume of the sensor. This metric aims to relate the mutual inductance, the maximum bandwidth and the total volume in terms of the previous defined metrics. Therefore,

$$\boxed{\kappa = w\eta_{G_{max}} \quad in\ (\frac{Vm}{A\ turn})} \tag{16}$$

where w stands for the width of the whole sensor. [14]

5.3 Design guidelines for coplanar pick-up coils

Design restrictions arise from general considerations regarding the nature of this kind of sensors, which must be pointed out to fully leverage their benefits.

[14] Since $V_{sensor} \approx A_{turn} w_{sensor}$

5.3.1 General constraints

In this section, the main geometrical constraints of the coplanar pick-up and their relationships to the electrical parameters are assessed. The purpose is to identify the key **adjustable** parameters.

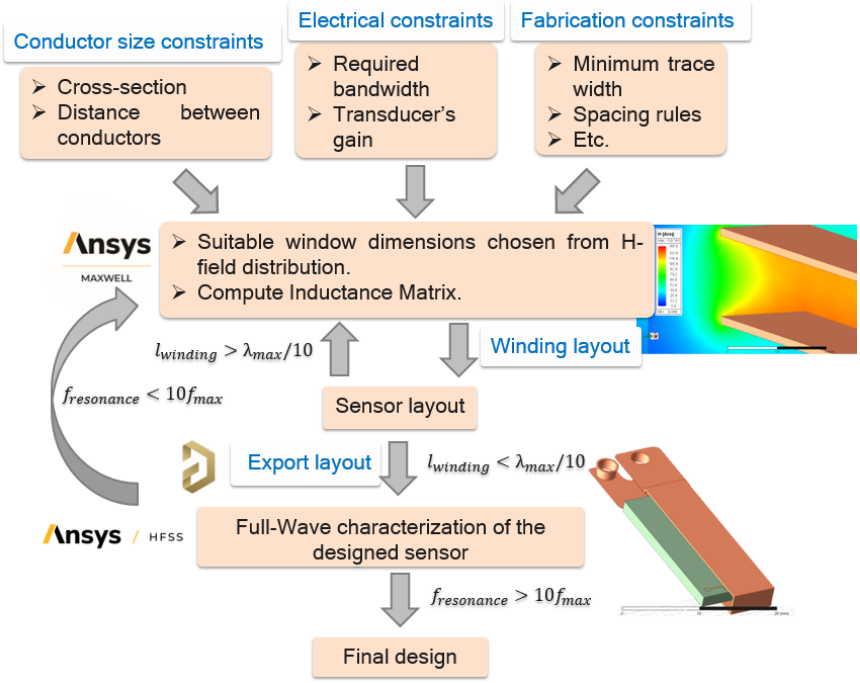

Figure 37: Suggested pick-up coil design workflow.

From the suggested general design workflow of these sensors, three different groups of constraints have been considered:

- **Conductor size constraints**. Directly related to the current density (J) and power board stack-up.
- **Electrical constraints**. Sets both, the minimum M and minimum required bandwidth of the sensor[15].
- **Fabrication constraints**. Which arise from the manufacturing process constraints.

[15]The maximum allowable insertion inductance sets additional constraints in the length of the sensing conductor. For a specific applications like "switch" current sensing, this specific approach -the PCB integration- naturally leads to tight design spaces

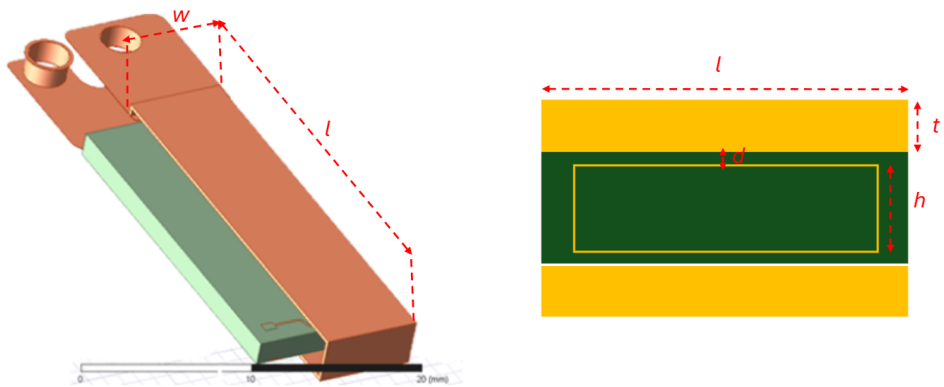

Figure 38: Key dimensions of the PUC B.

From the conductor size constraints, several geometrical parameters are set beforehand:

- **J**. Sets w and t of the sensed conductor [16].
- **Board stack-up**. Sets h.

Thorough evaluation of the effect of each dimension has on the performance of the pick-up coil requires extensive simulation effort. Analytical equations for every possible dimension are not feasible nor easily derived. Hence, the proposed guidelines must arise from the evaluation of simple equations governing the electrical behavior of the coplanar pick-up coil.

[16] It is not the purpose of this text to explain the design of this conductor.

	Adjust?	L_p	L_s	C_p	C_s	M	C_{CM}
h	✗	✓	✓	✓	✓	✓	✗
d	✗	✗	✗	✗	✗	✓	✓
t	✗	✓	✗	✗	✗	✗	✗
l	✓	✓	✓	✓	✓	✓	✓
w	✗	✓	✗	✓	✗	✓	✓
l_w	✓	✗	✓	✗	✓	✓	✓

Table 13: Dimensions and their relationship to electrical parameters of the pick-up coils.

1. **M**. The induced voltage at the pick-up coil's winding due the sensed current is

$$v = \underbrace{\frac{NA_{window}\mu}{l_m}}_{M=A_{window}N\eta_M} \frac{dI}{dt}$$

From above, the mutual inductance is

(a) Directly proportional to: N (which is directly proportional to the pick-up coil's winding length, l_w), A_{window} (h and l product).

(b) Inversely proportional to: l_m (which is proportional to h and d [17])

As already reported, h is set by the power board stack-up. Since d is the vertical distance from the nearest sensed conductor to the sensing winding, this parameter must be kept **as low as the manufacturing process allows** in order to obtain efficient designs (the field strength is higher as closer it is to the source of the field). Therefore the only two parameters which can be modified are l and l_w.

2. **Common mode capacitance,** C_{CM}. A rough approximation of the common mode capacitance as parallel plates can be used to

[17] This relationship arises from the curl of the magnetic field around the sensed conductor, regardless Ampère's law or Green's functions are considered.

understand the empirical behavior of this parasitic. This approximation holds as long as the pitch between turns is kept small (the top/bottom surfaces of the winding can be considered as plates), the total length of the winding is similar to the width of the sensed conductor (w) and the length of the cross-section of each turn is similar to the length of the sensed conductor (l).

$$C_{common} \approx 2\epsilon_r\epsilon_o\frac{A}{d} = 2\epsilon_r\epsilon_o\frac{wl}{d}$$

Since w is fixed by the current density, the only parameter which can be adjusted is l.

3. **Primary inductance,** L_p. Air coils arouse an analytical modeling challenge. The most general straight equation for external inductance is

$$L_p \approx \frac{N^2 A\mu}{l_m}$$

From above, the inductance is:

(a) Directly proportional to: N^2 (since the sensed coil behaves a single turn coil it can't be related -straightforward- to winding length itself), A_{window} (h and l product).

(b) Inversely proportional to: l_m (which is proportional to h and d)

The same constraints apply as already discussed for M.

4. **Secondary inductance,** L_s. As before

$$L_s \approx \frac{N^2 A\mu}{l_m}$$

Therefore:

(a) Directly proportional to: N^2, A_{window} (h and l product).

(b) Inversely proportional to: l_m (which is proportional to h)

The same constraints apply as already discussed for M.

5. **Primary capacitance,** C_p. As long as the coil's winding is neglected, it can be conceptually approximated as

$$C_p \approx \epsilon_r \epsilon_o \frac{A}{h} = \epsilon_r \epsilon_o \frac{wl}{h}$$

Since w and h are fixed, the only parameter which can be adjusted is l.

6. **Secondary capacitance,** C_s. Since turns ought to be placed as close as possible, the electric field "couples" with every single turn. Neglecting the real behavior of the electric field, if only immediately subjacent interactions, it can be -conceptually- approximated as the equivalent capacitance between two turns divided f

$$C_s \approx \epsilon_r \epsilon_o \frac{A_{eq}}{(N-1)p}$$

where A_{eq} stands for the equivalent area of each turn (which is related to the winding's "thickness", l and h) and p is the pitch between turns. (**In order to obtain compact rogowski-coils** p **must be kept as small as manufacturing constraints allows**). Therefore, N can be related to the total winding lenght, l_w.

5.3.2 Sensed conductor width influence on the mutual inductance

Given the geometrical constraints from Table.13, it is worth analyzing the influence the width of the sensed conductor has on the mutual inductance of the coil. Therefore, the winding layout region could be constrained.

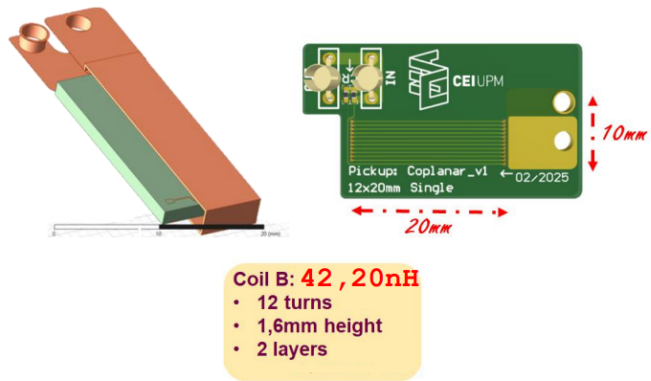

Figure 39: First design iteration of the PUC B.

For that purpose, a quasi-magnetostatic simulation is carried out in $Maxwell3D$ where width is swept from a nominal value from the design in Fig.39. In Fig.40 the relative deviation in the mutual inductance from the nominal value is depicted.

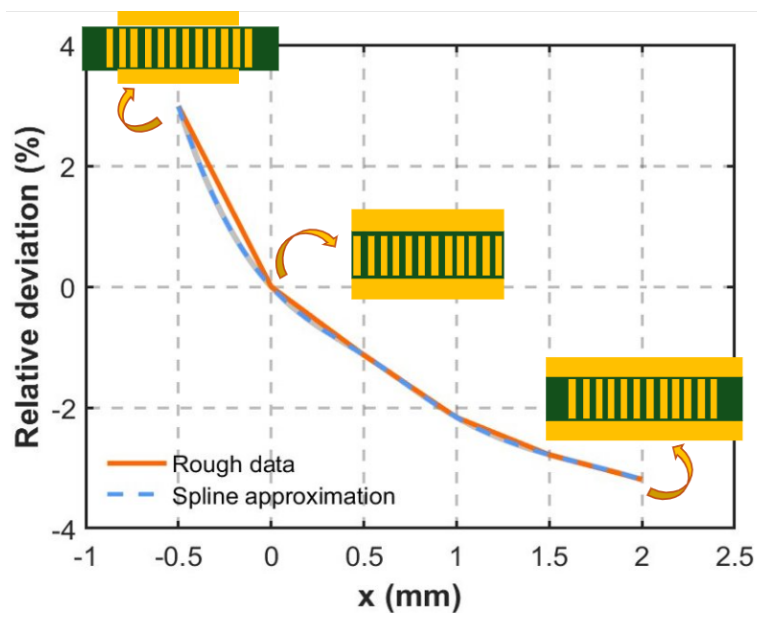

Figure 40: Relative mutual inductance variation with sensed conductor width.

Hence, in order to perform the layout of the pick-up coil's winding, the following must be considered:

1. **Current crowds towards conductor edges**. Current density crowds at conductor edges and corners due to the skin effect. At low enough frequencies, current distribution remains largely uniform.[18]

2. **Reducing conductor width enhances coupling**. The edge-dominated fields approach neighboring turns.

3. **Increasing conductor width reduces coupling**. As the edges move away and more turns lie over the weaker interior field.

4. **Green's function kernel for EM fields reveals the underlying mechanism from the fundamental $1/r$ behavior**.

5. **Uniform turns' coverage reduces voltage imbalance**. Extending sensed conductor coverage over all turns mitigates edge effects. Full coverage promotes uniform coupling with smoother flux linkage.

6. **Sensed conductor turns' coverage mitigates external coupling**. Covering turns reduces interference from external magnetic fields.

7. **Optimal sensed conductor width balances coupling and shielding when the turns cover the whole width**. Narrower width increases coupling and reduces common-mode capacitance but is more prone to pick up external fields. Wider conductors reduce coupling, increase common-mode capacitance and improve shielding.

[18] For conductors where the skin-depth is much smaller than its width, the coil's turns should be symmetrically located towards the edges.

6

PEEC Modeling

Executive Summary

In this chapter, a simplified PEEC solver in Matlab is discussed.
Main topics covered:

- Simplified PEEC solver applied to coplanar pick-up coils.
- Result's comparison with FEM simulations and small-signal measurements.

6.1 Motivation

This chapter examines the feasibility of a simplified PEEC solver for computing the mutual inductance in a coplanar pick-up coil arrangement. It covers the principles of the PEEC method and its implementation in *Matlab*.

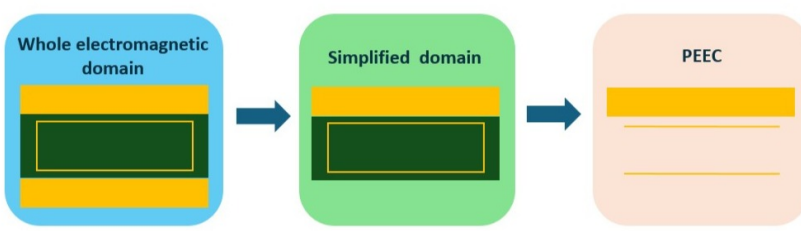

Figure 41: Simplified PEEC solver.

6.1.1 H field of an infinite strip with finite-width

A straight, infinitely long, zero-thickness conductive strip lying in the plane $z = 0$, occupying $x' \in [0, w_{\text{tot}}]$ and carrying a total current I in the $+\hat{\mathbf{y}}$ direction. Assume the current is distributed uniformly across

the strip width, so the linear current density (current per unit width) is

$$K = \frac{I}{w_{\text{tot}}} \quad (\text{A/m}).$$

47 The x-component of the magnetic flux density at the field point

$$P: \ \mathbf{r} = (x = w, \ y = 0, \ z = h), \qquad h > 0, \ 0 \le w \le w_{\text{tot}}.$$

For an infinitesimal filament at x' of width dx' the current is $dI = K\,dx'$. An infinite straight filament carrying dI produces at P a magnetic field of magnitude $\mu_0 dI/(2\pi R)$ with azimuthal direction and around the filament axis, where

$$R = \sqrt{(w - x')^2 + h^2}$$

is the perpendicular distance from the filament to P. In the $x{-}z$ cross section, the unit azimuthal vector is

54

$$\hat{\phi} = \frac{\hat{\mathbf{y}} \times \mathbf{R}}{R} = \frac{-h\,\hat{\mathbf{x}} + (w - x')\,\hat{\mathbf{z}}}{R},$$

with $\mathbf{R} = (w - x')\hat{\mathbf{x}} + h\hat{\mathbf{z}}$.

Thus the contribution of the filament to the horizontal field is

$$dB_x = \frac{\mu_0\,dI}{2\pi R}\,(\hat{\phi} \cdot \hat{\mathbf{x}}) = -\frac{\mu_0 K}{2\pi}\,\frac{h}{(w - x')^2 + h^2}\,dx'.$$

Integrating over the strip width gives

$$B_x(w, h) = -\frac{\mu_0 K}{2\pi} \int_0^{w_{\text{tot}}} \frac{h\,dx'}{(w - x')^2 + h^2}.$$

With the substitution $u = (w - x')/h$ (so $dx' = -h\,du$) and limits $u_1 = w/h, \ u_2 = (w - w_{\text{tot}})/h$, the integral reduces to an arctangent:

$$B_x(w, h) = \frac{\mu_0 K}{2\pi} \int_{u_1}^{u_2} \frac{du}{1 + u^2} = \frac{\mu_0 K}{2\pi}\left(\arctan\frac{w - w_{\text{tot}}}{h} - \arctan\frac{w}{h}\right).$$

Using $K = I/w_{\text{tot}}$,

$$B_x(w, h) = \frac{\mu_0 I}{2\pi w_{\text{tot}}}\left(\arctan\frac{w - w_{\text{tot}}}{h} - \arctan\frac{w}{h}\right).$$

6.1.2 Statement

In the previous section, a formula for the field created by a finite-width thin strip is derived, and which aims to describe the behavior of the magnetic field below or above the aforementioned strip. As already described in [Design of a High-Bandwidth Compact DC-Bus Embedded Planar Rogowski Coil for SiC MOSFET Current Sensing] this field can be used along with Faraday's law to obtain a formula for the mutual inductance between the strip and a rectangular filament spiral placed beneath/above with a given height $h_2 - h_1$, length l and placed at $x = w$

Starting from the magnetic field component $B_x(w, h)$ produced by a finite-width sheet of zero thickness carrying a uniform current density, the instantaneous field is proportional to the driving current $I(t)$:

$$B_x(w,h) = \frac{\mu_0 I(t)}{2\pi w_{\text{tot}}} \left[\arctan\left(\frac{w - w_{\text{tot}}}{h}\right) - \arctan\left(\frac{w}{h}\right)\right],$$

The time derivative of B_x is

$$\frac{\partial B_x}{\partial t} = \frac{\partial B_x}{\partial I}\frac{dI}{dt} = \frac{\mu_0}{2\pi w_{\text{tot}}} \left[\arctan\left(\frac{w - w_{\text{tot}}}{h}\right) - \arctan\left(\frac{w}{h}\right)\right] \frac{dI}{dt}.$$

By Faraday's law, the induced voltage on a straight conductor segment of length l located at lateral position w and spanning the vertical interval $h \in [h_1, h_2]$ is

$$v(t) = -\frac{d}{dt}\iint_{\mathcal{S}} B_x(w,h)\, dS = -\frac{dI}{dt} \underbrace{\left[\frac{l}{I}\int_{h_1}^{h_2} B_x(w,h)\, dh\right]}_{M(w)},$$

where $M(w)$ is the mutual inductance at position w.

Substituting $B_x(w, h)$ into the above gives

$$M(w) = \frac{\mu_0\, l}{2\pi w_{\text{tot}}} \int_{h_1}^{h_2} \left[\arctan\left(\frac{w - w_{\text{tot}}}{h}\right) - \arctan\left(\frac{w}{h}\right)\right] dh.$$

The integral above is analytically solvable only for a *given, fixed* w. The identity

$$\int \arctan\left(\frac{a}{h}\right) dh = h \arctan\left(\frac{a}{h}\right) + \frac{a}{2}\ln\left(h^2 + a^2\right)$$

with $a_1 = w - w_{\text{tot}}$ and $a_2 = w$, the following formula is obtained:

$$M(w) = \frac{\mu_0\, l}{2\pi w_{\text{tot}}} \left\{ \left[h \arctan\left(\frac{a_1}{h}\right) + \frac{a_1}{2} \ln\left(h^2 + a_1^2\right) \right]_{h_1}^{h_2} - \left[h \arctan\left(\frac{a_2}{h}\right) + \frac{a_2}{2} \ln\left(h^2 + a_2^2\right) \right]_{h_1}^{h_2} \right\}$$

If w is swept over a finite interval (nonzero width), a further integration over w is required. Since closed form formulas are prone to instability, numerical techniques are usually used to solve these integrals (e.g., discretized summation).

Nevertheless, this formula alone is valid as long as:

- The conductors can be approximated by thin strips, hence the cross section is small enough to be approximated by filaments.
- Each differential partition of a turn of the coil can be simplified as a thin rectangular closed spiral.

The previous statements hint at the outermost constraint of these formulas: it can't be extended to take account of high frequency effects (e.g., skin effect). It must be noted as well that the formulation itself arises from the field under quasi-static assumption.

6.2 The PEEC method

The interest surrounding the Partial Element Equivalent Circuit (PEEC) method has grown considerably since it is able to to model inductances without return current paths. Current research efforts are direct towards model order reduction (MOR) and computational acceleration [24].

For the sake of comparison, in Table 14, several popular EM numerical methods and their main characteristics are summarized. In contrast to the methods which rely on solving PDE, the PEEC method solves separate magnetic-field and electric-field integral equations. Therefore, the medium surrounding the conductors is not required to be discretized. In contrast to MoM, the PEEC method formulation inherently produces an equivalent lumped-element circuit.

Method	Equation Type	Variables	Domain	Material Handling	Computation	Characteristics / Applications
FDTD	Differential	E, H	TD	Linear anisotropic	Explicit time-stepping; High storage	Simple; explicit
FEM	Differential	E, H	TD / FD	Complex anisotropic	Large matrices; Moderate scalability	Flexible mesh; High accuracy
MoM	Integral	Density currents, charges	FD	Perfect Electric Conductors (Classic MoM)	Dense matrices; Extensive computation	Excels on open region problems (no absorbing boundaries)
PEEC	Integral	Currents, voltages	TD / FD	Conductors and simple dielectrics	Dense matrices; Extensive computation	Lumped-element description; Unified EM + circuital interpretation

Table 14: Comparison of EM methods

turnitin Página 82 de 116 - Engrega de integridad Identificador de la entrega trn:oid:::1:3331820056

6.2.1 Framework

The partial inductance concept was first introduced by Rosa [26] in 1908, later developed by Grover [27] in 1946, and polished by Hoer and Love [28] in 1965.

The PEEC method originated from inductance calculations for VLSI interconnects [29] performed by Albert E. Ruehli in 1972. The method addressed electrical interconnect problems by decomposing complex structures into basic partitions. For these partitions, inductances could be calculated. This approach eliminated the need to know the return current paths *a priori*, as required for loop inductance calculations.

6.2.2 Time domain PEEC formulation

Maxwell's differential equations in the time domain are given by

$$\nabla \times \mathbf{H}(\mathbf{r},t) = \frac{\partial \mathbf{D}(\mathbf{r},t)}{\partial t} + \mathbf{J}(\mathbf{r},t) \tag{17}$$

$$\nabla \times \mathbf{E}(\mathbf{r},t) = -\frac{\partial \mathbf{B}(\mathbf{r},t)}{\partial t} \tag{18}$$

$$\nabla \cdot \mathbf{B}(\mathbf{r},t) = 0 \tag{19}$$

$$\nabla \cdot \mathbf{D}(\mathbf{r},t) = q(\mathbf{r},t) \tag{20}$$

where $H(\mathbf{r},t)$ is the magnetizing field, $D(\mathbf{r},t)$ is the displacement field, $E(\mathbf{r},t)$ is the electric field, $B(\mathbf{r},t)$ is the magnetic field, $q(\mathbf{r},t)$ is the charge density, and $J(\mathbf{r},t)$ is the current density. In a linear isotropic medium, the fields H, B, E, and D satisfy the constitutive relations

$$\mathbf{B}(\mathbf{r},t) = \mu_0 \mu_r \mathbf{H}(\mathbf{r},t) \tag{21}$$

$$\mathbf{D}(\mathbf{r},t) = \varepsilon_0 \varepsilon_r \mathbf{E}(\mathbf{r},t) \tag{22}$$

A magnetic vector potential can be defined as

$$\mathbf{B}(\mathbf{r},t) = \nabla \times \mathbf{A}(\mathbf{r},t) \tag{23}$$

Substituting eq.(23) into eq.(18) yields:

$$\nabla \times [\mathbf{E}(\mathbf{r},t) + \frac{\partial \mathbf{A}(\mathbf{r},t)}{\partial t}] = 0 \tag{24}$$

This allows the definition of the electric scalar potential $\Phi(\mathbf{r},t)$ as

$$\mathbf{E}(\mathbf{r},t) + \frac{\partial \mathbf{A}(\mathbf{r},t)}{\partial t} = -\nabla \Phi(\mathbf{r},t) \tag{25}$$

$$\nabla \times \nabla \times \mathbf{A}(\mathbf{r},t) = \mu_0 \varepsilon_0 \frac{\partial}{\partial t}\left[-\frac{\partial \mathbf{A}(\mathbf{r},t)}{\partial t} - \nabla \Phi(\mathbf{r},t) \right] - \mu_0 \mathbf{J}(\mathbf{r},t) \tag{26}$$

Using the Laplacian identity

$$\nabla \times \nabla \times \mathbf{A}(\mathbf{r},t) = \nabla(\nabla \cdot \mathbf{A}(\mathbf{r},t)) - \nabla^2 \mathbf{A}(\mathbf{r},t) \tag{27}$$

and imposing the Lorenz gauge condition

$$\mathbf{A}(\mathbf{r},t) = -\mu_0 \varepsilon_0 \frac{\partial \Phi(\mathbf{r},t)}{\partial t} \tag{28}$$

The Helmholtz equation for the magnetic vector potential is obtained as

$$\nabla^2 \mathbf{A}(\mathbf{r},t) - \mu_0 \varepsilon_0 \frac{\partial^2 \mathbf{A}(\mathbf{r},t)}{\partial t^2} = -\mu_0 \mathbf{J}(\mathbf{r},t) \tag{29}$$

$$\nabla \cdot \left[-\frac{\partial \mathbf{A}(\mathbf{r},t)}{\partial t} - \nabla \Phi(\mathbf{r},t) \right] = \frac{q(\mathbf{r},t)}{\varepsilon_0} \tag{30}$$

The Helmholtz equation for the electric scalar potential is similarly obtained as

$$\nabla^2 \Phi(\mathbf{r},t) - \mu_0 \varepsilon_0 \frac{\partial^2 \Phi(\mathbf{r},t)}{\partial t^2} = -\frac{q(\mathbf{r},t)}{\varepsilon_0} \tag{31}$$

In a homogeneous medium, both $A(\mathbf{r},t)$ and $\Phi(\mathbf{r},t)$ admit closed-form solutions:

$$\mathbf{A}(\mathbf{r},t) = \frac{\mu_0}{4\pi}\int_{V'} G(\mathbf{r},\mathbf{r}')\mathbf{J}(\mathbf{r}',t')\,dV' \tag{32}$$

$$\Phi(\mathbf{r},t) = \frac{1}{4\pi\varepsilon_0}\int_{S'} G(\mathbf{r},\mathbf{r}')q(\mathbf{r}',t')\,dS' \tag{33}$$

$$G(\mathbf{r},\mathbf{r}') = \frac{e^{-jk|\mathbf{r}-\mathbf{r}'|}}{|\mathbf{r}-\mathbf{r}'|} \tag{34}$$

$$k = \omega\sqrt{\varepsilon_0\mu_0} \tag{35}$$

$$t' = t - \frac{|\mathbf{r}-\mathbf{r}'|}{c} \tag{36}$$

Here, $G(\mathbf{r},\mathbf{r}')$ is the Green's function for the Helmotz equation. In these expressions, t' denotes the time at which the source current (J) and charge (q) act as sources of A and Φ, respectively. It differs from t due to the finite speed of light in the medium, $c = 1/\sqrt{\mu\epsilon}$, which leads to the (36).

For electrically small problems, the quasi-static approximation can be applied, reducing (32) and (33) to (37) and (41), respectively.

$$\mathbf{A}(\mathbf{r},t) = \frac{\mu_0}{4\pi}\int_{V'} \frac{\mathbf{J}(\mathbf{r}',t')}{|\mathbf{r}-\mathbf{r}'|}\,dV' \tag{37}$$

$$\Phi(\mathbf{r},t) = \frac{1}{4\pi\varepsilon_0}\int_{S'} \frac{q(\mathbf{r}',t')}{|\mathbf{r}-\mathbf{r}'|}\,dS' \tag{38}$$

In electrical conductors, the relation between current density and electric field is expressed by

$$\mathbf{E}(\mathbf{r},t) = \frac{\mathbf{J}(\mathbf{r},t)}{\sigma} \tag{39}$$

where σ is the conductivity. Substituting (39) into the electric field equation (25) and considering an external electric field $E_0(\mathbf{r},t)$, the Electric Field Integral Equation (EFIE) is obtained as

$$\mathbf{E}_0(\mathbf{r},t) = \frac{\mathbf{J}(\mathbf{r},t)}{\sigma} + \frac{\partial}{\partial t}\frac{\mu_0}{4\pi}\int_{V'} \frac{\mathbf{J}(\mathbf{r}',t')}{|\mathbf{r}-\mathbf{r}'|}\,dV' + \nabla\Phi(\mathbf{r},t) \tag{40}$$

This holds for any point inside a conductor, where the electric scalar potential is related to the charge distribution by

$$\Phi(\mathbf{r}, t) = \frac{1}{4\pi\varepsilon_0} \int_{S'} \frac{q(\mathbf{r}', t')}{|\mathbf{r} - \mathbf{r}'|} \, dS' \tag{41}$$

Charge conservation is enforced through the continuity equation:

$$\nabla \cdot \mathbf{J}(\mathbf{r}, t) = -\frac{\partial q(\mathbf{r}, t)}{\partial t} \tag{42}$$

Assuming the charge resides only on conductor surfaces, for any point $\mathbf{r}$ inside the conductors, (42) becomes

$$\nabla \cdot \mathbf{J}(\mathbf{r}, t) = 0 \tag{43}$$

On their surfaces, applying the divergence theorem yields

$$\hat{\mathbf{n}} \cdot \mathbf{J}(\mathbf{r}, t) = \frac{\partial q(\mathbf{r}, t)}{\partial t} \tag{44}$$

where $\hat{\mathbf{n}}$ is the outward normal to surface S'.

The system of equations to be solved is made by equations (41), (40), (44) and (45). The unknowns in this problem are:

- $J(\mathbf{r}, t)$, the current density
- $q(\mathbf{r}, t)$, the surface charge density
- $\Phi(\mathbf{r}, t)$, the electric scalar potential of the conductors, expressed as a function of the charge density for $\mathbf{r} \in S_0$

6.2.3 Frequency domain PEEC formulation

The time-domain representation is effective under the quasi-static assumption, provided the problem is electrically small. For full-wave problems, however, the frequency-domain formulation is more suitable [30].

In the Laplace domain, the equations including propagation effects are given by

$$\mathbf{E}_0(\mathbf{r}, s) = \frac{\mathbf{J}(\mathbf{r}, s)}{\sigma} + s\frac{\mu_0}{4\pi}\int_{V'} \mathbf{J}(\mathbf{r}', s)\frac{e^{-s\tau}}{|\mathbf{r}-\mathbf{r}'|}\,dV' + \nabla\Phi(\mathbf{r}, s) \tag{45}$$

$$\Phi(\mathbf{r}, s) = \frac{1}{4\pi\varepsilon_0}\int_{S'} q(\mathbf{r}', s)\frac{e^{-s\tau}}{|\mathbf{r}-\mathbf{r}'|}\,dS', \quad \mathbf{r} \in S' \tag{46}$$

$$\nabla \cdot \mathbf{J}(\mathbf{r}, s) = 0, \quad \mathbf{r} \in V' \tag{47}$$

$$\hat{\mathbf{n}} \cdot \mathbf{J}(\mathbf{r}, s) = s\,q(\mathbf{r}, s), \quad \mathbf{r} \in S' \tag{48}$$

$$\tau = \frac{|\mathbf{r}-\mathbf{r}'|}{c} \tag{49}$$

where s is the Laplace variable. It should be noted that state-of-the-art PEEC formulations are typically solved with $s = j\omega$.

6.3 Procedure to solve

The numerical solution essentially follows a Galerkin weighted-residual approach [1]:

1. The unknowns $J(\mathbf{r}, s)$ and $q(\mathbf{r}, s)$ are approximated as weighted sums of a finite set of basis functions $b \in \mathbb{R}^3$ and $p \in \mathbb{R}$

$$\mathbf{J}(\mathbf{r}, s) \approx \sum_{n=1}^{N_v} \mathbf{b}_n(\mathbf{r}) I_n(s) \tag{50}$$

$$q(\mathbf{r}, s) \approx \sum_{m=1}^{N_s} p_m(\mathbf{r}) Q_m(s) \tag{51}$$

where $I_n(s)$ and $Q_m(s)$ are the basis function weights to be determined for each angular frequency s. N_v and N_s denote the number of volume and surface basis functions, with corresponding elementary volume and surface subregions.

[1] In Annex A a short overview of the theoretical basis that underlies this approach is presented.

2. Applying (45) and (46) to this system and implementing the Galerkin method yields

$$\Big\langle -\mathbf{E}_0(\mathbf{r},s) + \sum_{n=1}^{N_v} \frac{\mathbf{b}_n(\mathbf{r}) I_n(s)}{\sigma} + s\frac{\mu_0}{4\pi} \sum_{n=1}^{N_v} \int_{V_n} \frac{\mathbf{b}_n(\mathbf{r}') I_n(s) e^{-s\tau}}{|\mathbf{r}-\mathbf{r}'|}\, dV' + \nabla\Phi(\mathbf{r},s), \mathbf{b}_i(\mathbf{r})\Big\rangle = 0 \quad (52)$$

$$\Big\langle \Phi(\mathbf{r},s) - \frac{1}{4\pi\varepsilon_0} \sum_{m=1}^{N_s} \int_{S_m} \frac{p_m(\mathbf{r}') Q_m(s) e^{-s\tau}}{|\mathbf{r}-\mathbf{r}'|}\, dS', p_j(\mathbf{r})\Big\rangle = 0 \quad (53)$$

6.3.1 Partial inductances

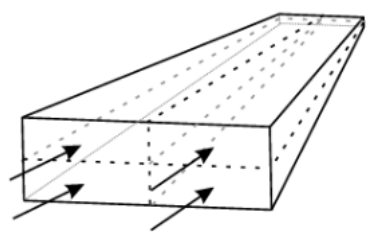

Figure 42: Partial element partition for volume cell [25].

The conductor volumes are discretized into N_v electrically small, orthogonal hexahedra (parallelepipeds) relative to the wavelength of the highest frequency of interest. Let ℓ_n and a_n denote the length and cross-section of volume V_n, respectively. The basis functions used to expand the current density are defined as

$$\mathbf{b}_n(\mathbf{r}) = \begin{cases} \frac{\hat{\mathbf{u}}_n}{a_n}, & \mathbf{r} \in V_n \\ 0, & \text{otherwise} \end{cases} \quad (54)$$

where $\hat{\mathbf{u}}_n$ is the unit vector indicating the current orientation in V_n. In this formulation, the basis function weight corresponds to the current flowing in V_n along $\hat{\mathbf{u}}_n$.

Hence, Garlerkin is applied to the Green's term. The partial inductance between two cells i and n is defined and computed through the double volume integral:

$$\left\langle s\frac{\mu_0}{4\pi}\sum_{n=1}^{N_v}\int_{V_n}\frac{\mathbf{b}_n(\mathbf{r}')I_n(s)e^{-s\tau}}{|\mathbf{r}-\mathbf{r}'|}dV', \mathbf{b}_i(\mathbf{r})\right\rangle =$$
$$= s\frac{\mu_0}{4\pi}\sum_{n=1}^{N_v} I_n(s)a_i a_n\left[\int_{V_i}\int_{V_n}\frac{e^{-s\tau}}{|\mathbf{r}_i-\mathbf{r}_n|}\hat{\mathbf{u}}_n\cdot\hat{\mathbf{u}}_i\,dV_n\,dV_i\right], \quad i=1,\ldots,N_v \tag{55}$$

$$L_{p_i,j}(s) = \frac{\mu_0}{4\pi}a_i a_j\int_{V_i}\int_{V_j}\frac{e^{-s\tau}}{|\mathbf{r}_i-\mathbf{r}_j|}\hat{\mathbf{u}}_i\cdot\hat{\mathbf{u}}_j\,dV_j dV_i \tag{56}$$

Therefore, the circuital nature of the PEEC method is revealed by the problem definition.

6.3.2 Inductance formula for Manhattan geometries

When the conductor dimensions are much smaller than the wavelength, the exponential term $e^{-s\tau}$ approaches unity, and the quasi-static approximation can be applied:

$$L_{p_i,j}(s) \approx L_{(qs)p_i,j} = \frac{\mu_0}{4\pi}a_i a_j\int_{V_i}\int_{V_j}\frac{1}{|\mathbf{r}_i-\mathbf{r}_j|}\hat{\mathbf{u}}_i\cdot\hat{\mathbf{u}}_j\,dV_j dV_i \tag{57}$$

For rectangular Manhattan geometries, analytical quasi-static partial inductance calculations are possible [29]. This approach offers a significant advantage: it produces nonsingular partial self-inductances, since it is based on the mutual coupling between two finite-length filaments. The total mutual partial inductance converges as more filaments for each conductor are considered.

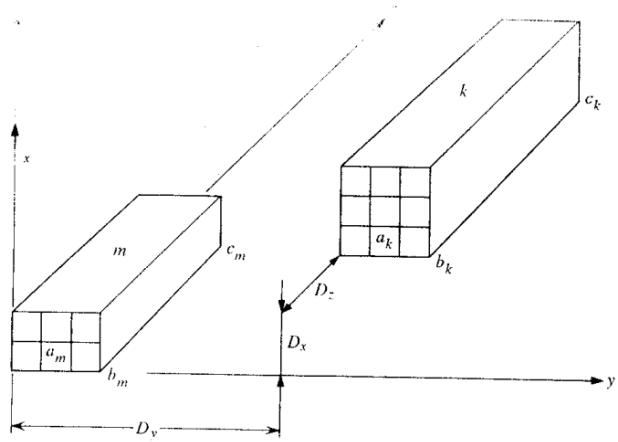

Figure 43: Mutual inductance for parallel current carrying conductors with rectangular cross-sections [29].

The total mutual partial inductance between two conductors with a rectangular cross-section [19] is given by:

$$L_{pkm} = \lim_{K\to\infty} \frac{1}{KM} \sum_{i=1}^{K} \sum_{j=1}^{M} L_{pf,ij}, \tag{58}$$

where the partial mutual inductance between two filaments is

$$\frac{L_{pf}^{ij}}{l_m} = \frac{\mu}{4\pi} \sum_{n=1}^{4} (-1)^{n+1} \left\{ g_n \log\left[g_n + \left(g_n^2 + r^2\right)^{1/2} \right] - \left(g_n^2 + r^2\right)^{1/2} \right\}, \tag{59}$$

where $g_1 = 1+p$, $g_2 = 1+p-\nu$, $g_3 = p-\nu$, and $g_4 = p$. The normalizations are defined as $\nu = l_k/l_m$, $p = \Delta z/l_m$, and $r = \sqrt{(x_m - x_k)^2 + (y_m - y_k)^2} / l_m$

6.4 Suggested simplified PEEC algorithm

The proposed approach to calculate the mutual inductance in the coplanar arrangement relies on calculating the mutual inductance between the top sensed conductor and each winding partition where the current

[19] **Where the current vector points in the same direction as the normal vector of that surface.**

points in the same direction as the current through the sensed conductor. **This was already depicted in Fig.42**. Therefore the structure can be greatly simplified.

A uniform square grid partition for the meshing of all the conductors has been employed [20]. In order to increase the sensitivity to the coupling between different partitions, the maximum length of each element has been set to $0.2mm$. This value is chosen according to the expected per unit length mutual coupling as shown in Fig.45. The whole code can be found in Appendix D.

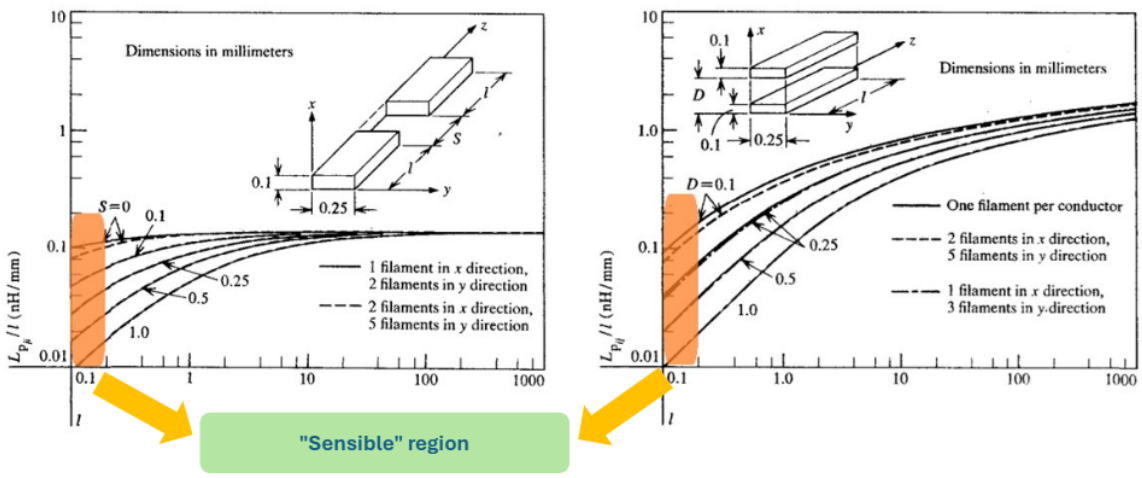

Figure 44: Mutual inductance per length unit [29].

In order to test the performance of the proposed PEEC solver, the results are compared to the ones obtained in [4]. In Table.15, the considered conductors' dimensions and positions are summarized.

[20] From Fig.43 the cross-section has the same number of divisions in each direction

	Sensed Conductor	Top Conductor	Bottom Conductor
Dimensions (mm)			
Size x	0.50	0.035	0.035
Size y	2.50	0.15	0.15
Size z	11.83	11.83	11.83
Origin (x-coordinate, mm)			
x_0	1.935	1.465	0.000
X-Differences (mm)			
$\Delta x_{Sensed-top}$		0.470	
$\Delta x_{top-down}$		1.465	
Other parameters			
N		8	
$Distance_{turn-turn}$		$0.3mm$	
$Axis_{divisions}$	3	4	2

Table 15: Dimensions and x–spacing of the three rectangular conductors

Algorithm 1 Computation of Mutual Inductance M

Require: Number of turns N, distance between turns, prism origins and sizes
Ensure: Total mutual inductance M

```
Initialize M ← 0
Subdivide the main U-prism into smaller cells
Generate and simplify vertical line representations of the U-prism → linesA
for k = 1 to N do
    Position the upper and lower prisms at separation (k − 1)
    Subdivide the upper and lower prisms into smaller cells
    Generate and simplify vertical line representations → linesB, linesBdown
    Compute mutual inductances:
    M_up ← computeMRuehli(linesA, linesB)
    M_down ← computeMRuehli(linesA, linesBdown)
    Accumulate contributions: M ← M + M_up + M_down
end for
return 2M
```

6.4.1 Results

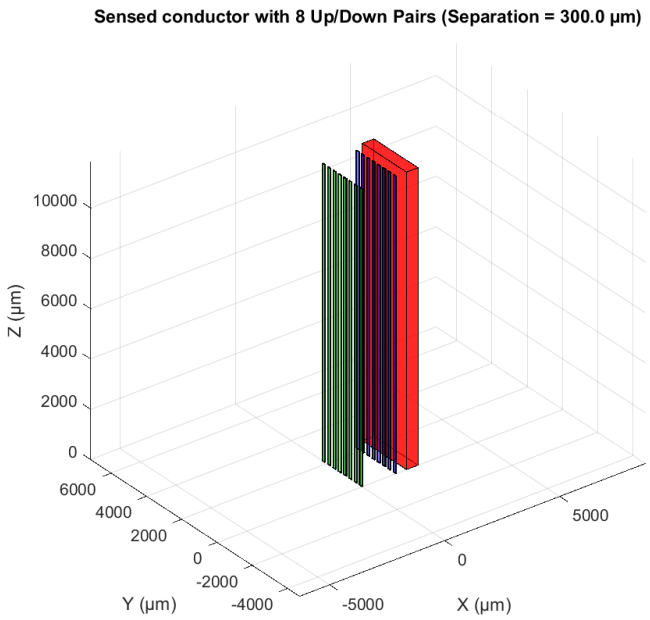

Figure 45: 3D render of the evaluated layout.

	FEM @ 100 kHz	Small-signal @ 100 kHz	PEEC
M [nH]	28.6	30.2	2*20.40

Table 16: Comparison of mutual inductance extracted by FEM, small-signal model at $100kHz$ and the suggested PEEC solver

From Table.16 the simplified PEEC method yields a 35% relative error compared to the measured mutual inductance value. As already discussed in the previous chapter, the relative position between the windings and the sensed conductor might explain up to ±2% considering there is an error in the position of the windings. Nevertheless, the main source of uncertainty might be the skin effect itself. From the 1-D Helmhotz equation, the normalized current density can be described as [31]:

$$\frac{|J(x)|}{J_{\mathrm{DC}}} = \frac{1}{2}\,\frac{w}{\delta}\,\frac{\cosh\left(\frac{x}{\delta}\right) + \cos\left(\frac{x}{\delta}\right)}{\cosh\left(\frac{x}{\delta}\right) - \cos\left(\frac{x}{\delta}\right)}.$$

where $J(x)$ is the local current density at depth x [A/m^2], J_{DC} is the uniform (dc) current density [A/m^2], w is the thickness of the conductor [m], x is the distance from the conductor center [m] and δ is the skin depth [m].

$$\delta = \sqrt{\frac{\rho}{\pi f \mu}}.$$

40 where ρ is the electrical resistivity [Ω·m], f is the frequency [Hz] and μ is the magnetic permeability [H/m].

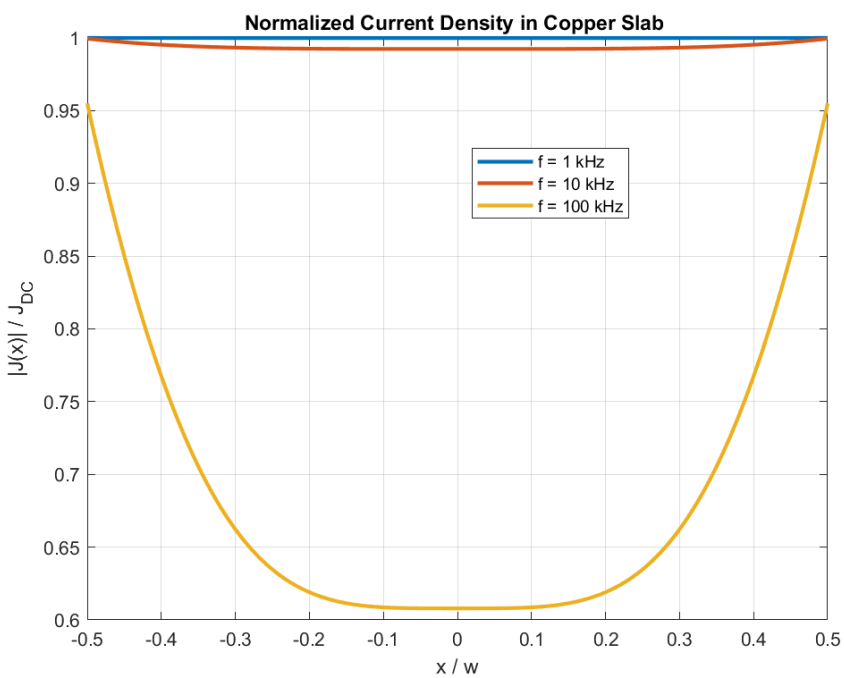

Figure 46: Normalized current density distribution with frequency in the simulated sensed conductor.

Remarks on the simulation's result

From Fig.46 for $100kHz$ the current density falls to nearly half its normalized value when the distance to the center is inferior to $\pm 20\%$ the total conductor's thickness. **Since most of the current flows through the edges of the sensed conductor, the contribution of the partial elements around the center of the sensed conductor have nearly half the influence to the total mutual inductance**. This might explain most of the error achieved. This is something yet to be proved and which hasn't been covered in this thesis.

7

Conclusions and Future Work

7.1 Contributions and alignment with SDGs

The increasing adoption of wide-bandgap (WBG) semiconductor technologies, such as silicon carbide (SiC) and gallium nitride (GaN), is transforming the design of switched-mode power converters. These devices enable higher switching frequencies and improved efficiency, but they also demand advanced sensing solutions to ensure accurate control and protection. This research addresses this challenge by developing a *high-bandwidth isolated PCB-integrated current sensor*. The innovation contributes directly to the efficiency, scalability, and sustainability of power electronics, aligning with multiple **United Nations Sustainable Development Goals (SDG)**.

The proposed current sensing solution integrates isolation and high-bandwidth performance within the PCB itself, offering a cost-effective, compact, and reliable alternative to conventional discrete sensors. Its technical contributions include:

- Demonstrated that PCB PUC are feasible current sensors with enhanced bandwidth for accurate isolated measurement in WBG-based converters.
- Provided validated models, experimental benchmarks and design guidelines to support future adoption in industry and research.
- Opened a path toward systematic sensor optimization through combined analytical, numerical and experimental methods.

This research demonstrates that innovation at the component level—such as current sensing—can have a broad systemic impact on sustainability. By improving the performance and manufacturability of WBG-based power converters, the developed PCB-integrated current sensor

strengthens the link between **technological advancement and sustainable development**. These outcomes strengthen the reliability and scalability of power converters for renewable energy, electrified transportation, and sustainable industrial systems. The work highlights how engineering research can accelerate progress toward the **UN 2030 Agenda** by addressing challenges in energy efficiency, industrial innovation, responsible production, climate change mitigation, and environmental preservation. Indeed, it is aligned with the following SDG:

- **SDG 7 – Affordable and Clean Energy:** Improved sensing enhances the efficiency of renewable energy converters, supporting reliable access to clean energy.
- **SDG 9 – Industry, Innovation, and Infrastructure:** PCB-integrated sensing fosters scalable, manufacturable solutions that advance next-generation power electronics for electric mobility and smart grids.
- **SDG 12 – Responsible Consumption and Production:** Increased converter efficiency reduces resource consumption, waste, and the environmental footprint of energy conversion systems.
- **SDG 13 – Climate Action:** By minimizing power losses, the research contributes to lower greenhouse gas emissions and supports global decarbonization strategies.
- **SDG 15 – Life on Land:** Indirectly contributes to biodiversity protection by enabling cleaner energy transitions that reduce land degradation from fossil fuel use.

7.1.1 Future Research Lines

The work developed in this thesis opens several avenues for future research:

- **Enhanced common-mode rejection**: Future designs may explore fully differential layouts or hybrid approaches that combine Rogowski coils with auxiliary shielding or compensation windings to improve robustness against high-dv/dt environments.
- **Advanced integration with power converters**: Embedding the sensors closer to switching devices or within PCB busbars

could further minimize parasitics and provide higher-fidelity current measurements.

- **Improved PEEC formulations**: The simplified PEEC solver developed in this work could be extended to full-wave non-Manhattan geometries, enabling more accurate modeling of the layouts.
- **Automated design workflows**: Coupling FEM and PEEC simulations with optimization algorithms would allow automatic exploration of coil geometries under predefined figures of merit.

Project Schedule

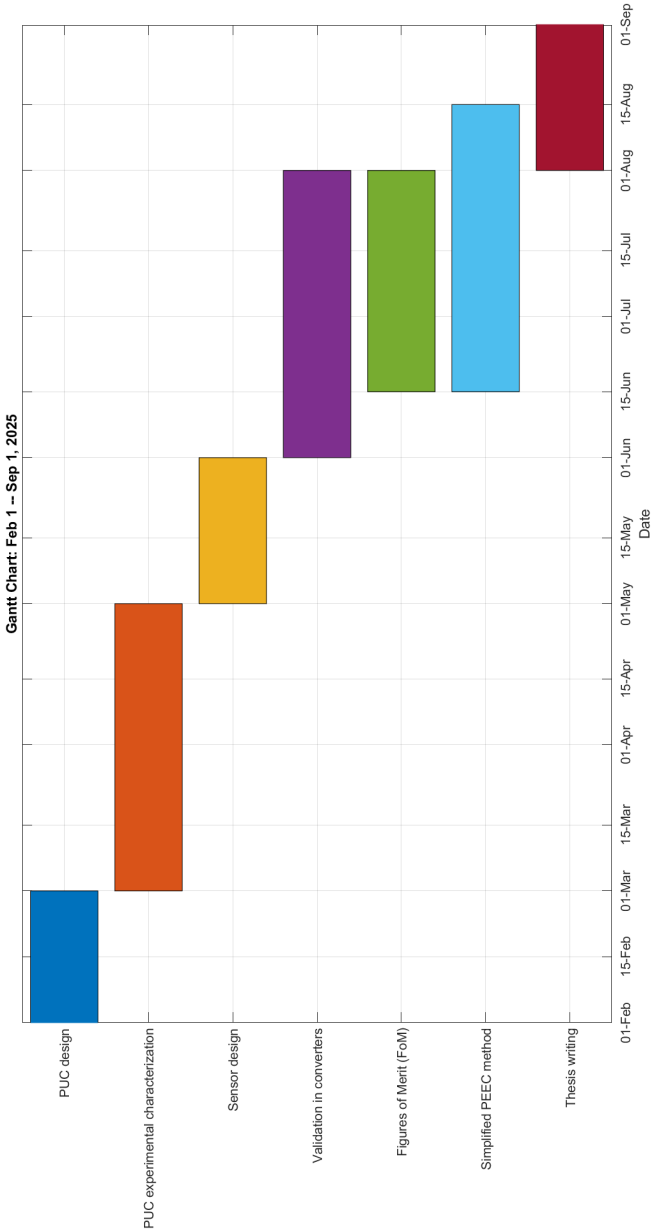

Figure 47: Gantt chart.

Budget

Except for the materials needed to develop the prototype, the remaining material resources are assumed to be fully amortized. This distinction applies strictly to instruments (power supplies, computers, etc.). The enrollment cost in the course is not considered. However, its inclusion as an administrative expense could be discussed.

	Concept	**Cost [€]**
	Resources	
1	PUC prototypes	47.20
2	GaN Buck Prototype	32.40
3	SiC PFC Boost Prototype	50.35
Subtotal		**129.95**
	Personnel	
1	Monthly expenses [€/month]	600
2	Time [months]	6
Subtotal		**3600.00**
	Total	
		3729.95

Table 17: Summary of costs: resources, personnel, and total.

8

Appendix A: On the tracking of pulses

Given the system

$$H(s) = \frac{Ms}{1 + s\tau},$$

The time domain impulse response can be derived from the inverse Laplace transformation as partial fractions.

$$h(t) = \frac{M}{\tau}\delta(t) - \frac{M}{\tau^2}e^{-t/\tau}u(t).$$

Frequency-domain condition for exact tracking

For an input $x(t)$, the output in the frequency domain follows

$$Y(s) = H(s)X(s).$$

If the system *perfectly tracks* the input up to a scaling constant K, then

$$Y(s) = KX(s),$$

which requires

$$H(s) = K$$

Therefore, for the input's signal bandwidth $X(s = j\omega)$, a necessary condition for exact tracking is that $H(j\omega)$ is constant in magnitude and no phase lag is introduced.

Transfer function analysis

For the system

$$H(j\omega) = \frac{Mj\omega}{1 + j\omega\tau}.$$

Is not constant near $\omega \sim 1/\tau$. In fact, at $\omega = 1/\tau$,

$$|H(j\omega)| = \frac{M/\tau}{\sqrt{2}}, \qquad \angle H(j\omega) = 45^\circ,$$

Therefore, frequencies around the cut-off frequency are attenuated and phase-shifted.

Input edge spectrum

A pulse edge with 10–90% rise time t_r has significant spectral content up to approximately [21]

$$\omega_{\max} \sim \frac{1}{t_r}.$$

then

$$\omega_{\max} \sim \frac{1}{t_r} \approx \frac{1}{2.2\tau}.$$

Hence, $\omega_{\max}$ is of the same order as $1/\tau$. Therefore, the input spectrum lies in the region where $H(j\omega)$ introduces phase lag.

Step Response of the rogowski coil

For a unit step input, $I(s) = 1/s$, the reconstructed current is:

$$V(s) = H_{\text{total}}(s) \cdot I(s) = \frac{Ms}{1 + sR_sC_s} \cdot \frac{1}{s} = \frac{M}{1 + sR_sC_s}.$$

Taking the inverse Laplace transform

$$v(t) = M\left(1 - e^{-t/(R_sC_s)}\right), \quad t \geq 0.$$

The 10-90% rise time can be derived as

$$t_r \approx 2.2\, R_sC_s.$$

[21] This approximation arises from Fourier signal decomposition, neglecting the fact the pulse itslef is not periodic.

Relation to cut-off frequency

The –3 dB bandwidth of the RC integrator is

$$f_c = \frac{1}{2\pi R_s C_s}. \tag{60}$$

Multiplying rise time by bandwidth

$$t_r \cdot f_c \approx 2.2 R_i C_i \cdot \frac{1}{2\pi R_i C_i} \approx 0.35, \tag{61}$$

Which leads to the relation

$$\boxed{t_r \approx \frac{0.35}{f_c}}.$$

9

Appendix B: Review of concepts applied in PEEC

Variational Methods

Many differential equations can be reformulated as variational problems, where the goal is to find a function that minimizes (or makes stationary) a certain integral. Such problems are called variational problems, and the techniques to reduce a differential equation to a variational problem are called variational methods.

In the calculus of variations, we seek a function $y(x)$ that makes a functional

$$I(y) = \int_a^b F(x, y(x), y'(x))\, dx$$

stationary. A variation δy represents an infinitesimal change in y while keeping x fixed. The first variation of $I(y)$ is

$$\delta I = \int_a^b \left(\frac{\partial F}{\partial y} \delta y + \frac{\partial F}{\partial y'} \delta y' \right) dx,$$

and the necessary condition for $I(y)$ to have an extremum is $\delta I = 0$. Applying integration by parts and assuming $\delta y(a) = \delta y(b) = 0$ yields the Euler-Lagrange equation:

$$\frac{\partial F}{\partial y} - \frac{d}{dx}\left(\frac{\partial F}{\partial y'}\right) = 0.$$

Weighted Residual Methods (WRM)

The Weighted Residual Method generalizes variational approaches, allowing treatment of PDEs even when a functional does not exist or when boundary conditions are inhomogeneous. Given a PDE

$$Lu = f,$$

the unknown solution $u(x)$ is approximated as

$$u(x) \approx \sum_{n=1}^{N} a_n u_n(x),$$

where $u_n(x)$ are known basis functions and a_n are coefficients to be determined. The residual is defined as

$$R = Lu - f,$$

and the weighted residual condition requires

$$\int w_m R \, dv = 0$$

for a set of test functions w_m. The Galerkin method chooses the test functions equal to the basis functions: $w_m = u_m$. This orthogonality condition ensures a unique solution within the approximation space.

Green Functions

For a linear operator L, the Green function $G(x, \xi)$ satisfies

$$LG(x, \xi) = \delta(x - \xi)$$

with the same boundary conditions as the PDE. Using $G(x, \xi)$, the exact solution can be written as

$$u(x) = \int G(x, \xi) f(\xi) \, d\xi,$$

which guarantees the existence and uniqueness of the solution.

Difference with PEEC Method

In methods such as PEEC (Partial Element Equivalent Circuit), the PDE is rewritten as an integral equation using Green functions. This is convenient when analytical Green functions are unavailable or the geometry is complex. The "new" unknown is expanded and solved using similar techniques as already described.

Unlike the "basic" weighted residual method:

- The residual is already expressed in integral form.

- Uniqueness is not automatically guaranteed by the Green function alone. It depends on the choice of basis and test functions.
- The uniqueness property is determined by the discretization, not just the integral kernel.

10

Appendix C: Matlab Code for Simplified PEEC

main.m — MATLAB script for computing M

```
N = 8;
separation = 0.3e-3;
divisions = 4;

origin_U = [1.5e-3 + 35e-6 + 0.4e-3, 0, 0];
size_U   = [0.5e-3, 2.5e-3, 11.83e-3];

origin_up   = [1.5e-3 - 35e-6, 0, 0];
size_up     = [35e-6, 0.15e-3, 11.83e-3];

origin_down = [0, 0, 0]*1e-6;
size_down   = size_up;

M = 0;

divU = subdivide_prismU(origin_U, size_U, 0.2e-3); % maximum 1mm length
[~, length_divU] = size(divU); % is 1x2 vector

linesAmask = [];
linesA = [];
for k = 1:length_divU
    linesAmask = [linesAmask, ...
        generateVerticalLines(divU(k).origin, divU(k).size, 3)];
end
linesA = simplify_cellv2(linesAmask);

for k = 1:N
    origin_up_k   = origin_up   + [0, (k-1)*separation, 0];
    origin_down_k = origin_down + [0, (k-1)*separation, 0];
    divup = subdivide_prismv2(origin_up_k, size_up, 0.2e-3);
    [~, length_divup] = size(divup); % is 1x2 vector
    divdown = subdivide_prismv2(origin_down_k, size_down, 0.2e-3);
    [~, length_divdown] = size(divdown); % is 1x2 vector

    linesB = [];
    linesBmask = [];
    for i = 1:length_divup
        linesBmask = [linesBmask, ...
            generateVerticalLines(divup(i).origin, divup(i).size, 4)];
    end
    linesB = simplify_cellv2(linesBmask);

    linesBdown = [];
    linesBdownmask = [];
```

```
    for j = 1:length_divdown
        linesBdownmask = [linesBdownmask, ...
            generateVerticalLines(divdown(j).origin, divdown(j).size, 2)];
    end
    linesBdown = simplify_cellv2(linesBdownmask);

    M_up(k) = computeMRuehli(linesA, linesB);
    M_down(k) = computeMRuehli(linesA, linesBdown);
    M = M + M_up(k) + M_down(k);
end
```

computeMRuehli.m — MATLAB function to compute mutual inductance between line sets

```
function M = computeMRuehli(linesA, linesB)

% lines{1}(1,1) x line 1 "origin", lines{1}(2,1) x "end"

iterA = length(linesA);
iterB = length(linesB);

mu = 4*pi*1e-7; % Vacuum
L_base = 0;

for i = 1:iterA
    for j = 1:iterB

        lengthA = linesA{i}(2,3) - linesA{i}(1,3);
        lengthB = linesB{j}(2,3) - linesB{j}(1,3);
        offsetBA = linesB{j}(1,3) - linesA{i}(1,3);

        v = lengthB / lengthA;
        p = offsetBA / lengthA;

        x = linesA{i}(1,1) - linesB{j}(1,1);
        y = linesA{i}(1,2) - linesB{j}(1,2);

        r = sqrt(x^2 + y^2) / lengthA;

        g1 = 1 + p;
        g2 = 1 + p - v;
        g3 = p - v;
        g4 = p;

        L1 = (mu/(4*pi)) * (g1 * log(g1 + sqrt(g1^2 + r^2)) - sqrt(g1^2 + r^2));
        L2 = -1*(mu/(4*pi)) * (g2 * log(g2 + sqrt(g2^2 + r^2)) - sqrt(g2^2 + r^2));
        L3 = (mu/(4*pi)) * (g3 * log(g3 + sqrt(g3^2 + r^2)) - sqrt(g3^2 + r^2));
        L4 = -1*(mu/(4*pi)) * (g4 * log(g4 + sqrt(g4^2 + r^2)) - sqrt(g4^2 + r^2));

        L_base = L_base + (L1 + L2 + L3 + L4) * lengthA;
    end
end

M = 1 / (iterA * iterB) * L_base;

end
```

subdivide_prismU.m — MATLAB function for subdividing a prism

```
function [subcells, config] = subdivide_prismU(origin, size_vec, fixedMaxL)
    % origin: [x0, y0, z0] = [T_start, W_start, L_start]
    % size_vec: [T0, W0, L0] = prism dimensions
    % fixedMaxL: max allowed cell length (e.g., lambda/20)

    T0 = size_vec(1);
    W0 = size_vec(2);
    L0 = size_vec(3);

    best_config = [];
    max_cells = 0;

    nT = floor(T0 / 100e-6);
    nW = floor(W0 / 25e-6);
    nL = floor(L0 / fixedMaxL);

    T_adj = T0 / nT;
    W_adj = W0 / nW;
    L_adj = L0 / nL;

    rTW_adj = T_adj / W_adj;
    rLW_adj = L_adj / W_adj;

    best_config = struct('nT', nT, 'nW', nW, 'nL', nL, ...
                         'T', T_adj, 'W', W_adj, 'L', L_adj, ...
                         'rTW', rTW_adj, 'rLW', rLW_adj);

    % Generate subcells
    idx = 1;
    for i = 0:best_config.nT - 1
        for j = 0:best_config.nW - 1
            for k = 0:best_config.nL - 1
                origin_ijk = origin + [i, j, k] .* [best_config.T, best_config.W, best_config.L];
                subcells(idx).origin = origin_ijk;
                subcells(idx).size   = [best_config.T, best_config.W, best_config.L];
                idx = idx + 1;
            end
        end
    end

    config = best_config;
end
```

generateVerticalLines.m — MATLAB function to generate vertical lines in a prism

```
function lines = generateVerticalLines(origin_U, size_U, ak)
%GENERATEVERTICALLINES Generate vertical lines in a rectangular prism.
%
%   lines = generateVerticalLines(origin_U, size_U, ak)
%
%   Inputs:
%     origin_U : 1x3 vector [x0, y0, z0] - Origin of the prism
%     size_U   : 1x3 vector [dx, dy, dz] - Dimensions of the prism
%     ak       : Integer - Number of divisions along x and y
%
%   Output:
%     lines    : Cell array - Each cell contains a 2x3 matrix representing
%                a line from (x, y, z0) to (x, y, z1)

    % Unpack inputs
    x0 = origin_U(1);
    y0 = origin_U(2);
    z0 = origin_U(3);

    dx = size_U(1);
    dy = size_U(2);
    dz = size_U(3);

    step_x = dx / ak;
    step_y = dy / ak;

    % Compute step sizes and point values along x and y
    x_vals = x0 : step_x : x0 + dx;
    y_vals = y0 : step_y : y0 + dy;

    % Top surface z-value
    z1 = z0 + dz;

    % Initialize cell array
    index = 1;

    % Loop over grid points in x-y and create vertical lines
    for i = 1:length(x_vals)
        for j = 1:length(y_vals)
            x = x_vals(i);
            y = y_vals(j);
            lines(index).origin = [x, y, z0];
            lines(index).size   = [x, y, z1];  % 2x3 matrix
            index = index + 1;
        end
    end
end
```

simplify_cellv2.m — MATLAB function to extract unique lines from a struct array

```
function uniqueLines = simplify_cellv2(lines)

% === Convert each line to 1x6 row, round to remove float noise ===
numLines = numel(lines);
lineMatrix = zeros(numLines, 6);

for i = 1:numLines
    % Concatenate from and to points into one row
    fullLine = [lines(i).origin, lines(i).size];

    % Round to nanometer precision (adjust if needed)
    % fullLine = round(fullLine * 1e12) / 1e12;

    lineMatrix(i, :) = fullLine;
end

% === Use unique on the rounded rows ===
[~, ia] = unique(lineMatrix, 'rows');

% === Extract unique lines from original struct ===
uniqueLines = struc2cell_own(lines(ia));

end
```

References

[1] J. W. Kolar, F. Krismer, Y. Lobsiger, J. Muhlethaler, T. Nussbaumer, and J. Minibock, "Extreme efficiency power electronics," in Conference on Integrated Power Electronics Systems (CIPS), 2012.

[2] N. Kaminski, "State of the Art and the Future of Wide Band-Gap Devices," in IEEE European Conference on Power Electronics and Applications (EPE), 2009.

[3] T. P. Chow, "Wide Bandgap Semiconductor Power Devices for Energy Efficient Systems," in IEEE Workshop on Wide Bandgap Power Devices and Applications (WiPDA), 2015.

[4] P. S. Niklaus, D. Bortis, and J. W. Kolar, "Beyond 50 MHz Bandwidth Extension of Commercial DC-Current Measurement Sensors With Ultra-Compact PCB-Integrated Pickup Coils," IEEE Transactions on Industry Applications, vol. 58, no. 4, pp. 5026–5041, 2022, doi: 10.1109/TIA.2022.3164865.

[5] S. Zhang, W. Song, H. Cao, T. Tang, and Y. Zou, "A Digital-Twin-Based Health Status Monitoring Method for Single-Phase PWM Rectifiers," IEEE Transactions on Power Electronics, vol. 38, no. 11, pp. 14075–14087, 2023, doi: 10.1109/TPEL.2023.3307415.

[6] S. Sanfilippo, "Hall probes: Physics and application to magnetometry," arXiv preprint arXiv:1103.1271, 2011. [Online]. Available: https://arxiv.org/pdf/1103.1271

[7] J. Frounchi, M. Demierre, Z. Randjelovic, and R. S. Popovic, "Integrated Hall sensor array microsystem," in IEEE International Solid-State Circuits Conference, 2001, pp. 248–249.

[8] B. Drafts, "New Magnetoresistive current sensor improves power electronics performance," Sensors, Sep. 1999.

[9] M. Fritsch and M. Wolter, "High-Frequency Current Transformer Design and Construction Guide," IEEE Transactions on Instrumentation and Measurement, vol. 71, pp. 1–9, 2022, doi: 10.1109/TIM.2022.3177189.

[10] F. Costa, E. Laboure, F. Forest, and C. Gautier, "Wide Bandwidth, Large AC Current Probe for Power Electronics and EMI Measurement," IEEE Transactions on Industrial Electronics, vol. 44, no. 4, pp. 502–511, 1995.

[11] T&M Research Products Inc., "Series SDN/SSDN-414 datasheet," 2024. [Online]. Available: Online; accessed Jan. 2024

[12] C. M. Johnson and P. R. Palmer, "Current measurement using compensated coaxial shunts," IEE Proceedings Science, Measurement and Technology, vol. 141, no. 6, pp. 471–480, 1994.

[13] W. Rogowski and W. Steinhaus, "Die Messung der magnetischen Spannung," Archiv für Elektrotechnik, vol. 1, no. 4, pp. 141–150, 1912, doi: 10.1007/BF01656479. [Online]. Available: http://link.springer.com/article/10.1007/BF01656479

[14] A. P. Chattock, "On a Magnetic Potentiometer," Proceedings of the Physical Society of London, vol. 9, no. 1, pp. 23–26, 1887, doi: 10.1088/1478-7814/9/1/305

[15] J. Wang et al., "Infinity Sensor: Temperature Sensing in GaN Power Devices using Peak di/dt," in IEEE Energy Conversion Congress and Exposition (ECCE), 2018, pp. 884–890, doi: 10.1109/ECCE.2018.8558287.

[16] H. C. P. Dymond, Y. Wang, S. Jahdi, and B. H. Stark, "Probing Techniques for GaN Power Electronics: How to Obtain 400+ MHz Voltage and Current Measurement Bandwidths without Compromising PCB Layout," in PCIM Europe 2022, 2022, doi: 10.30420/565822010.

[17] L. Zhao, J. D. van Wyk, and W. G. Odendaal, "Planar embedded pick-up coil sensor for power electronic modules," in IEEE Applied Power Electronics Conference and Exposition (APEC), 2004, pp. 945–951, doi: 10.1109/APEC.2004.1295936.

[18] J. N. Fritz, C. Neeb, and R. W. De Doncker, "A PCB integrated differential Rogowski coil for non-intrusive current measurement featuring high bandwidth and dv/dt immunity," 2015. [Online]. Available: https://eldorado.tu-dortmund.de/items/818eb3f5-3620-4ec8-8d43-3b48428589cb

[19] N. Karrer and P. Hofer-Noser, "A new current measuring principle for power electronic applications," in 11th International Symposium on Power Semiconductor Devices and ICs, 1999, pp. 279–282.

[20] D. Gerber, T. Guillod, R. Leutwyler, and J. Biela, "Gate Unit With Improved Short-Circuit Detection and Turn-Off Capability for 4.5-kV Press-Pack IGBTs Operated at 4-kA Pulse Current," IEEE Transactions on Plasma Science, vol. 41, no. 10, pp. 2641–2648, 2013, doi: 10.1109/TPS.2013.2280379.

[21] T. Funk and B. Wicht, "A fully integrated DC to 75 MHz current sensing circuit with on-chip Rogowski coil," in IEEE Custom Integrated Circuits Conference (CICC), 2018, pp. 1–4, doi: 10.1109/CICC.2018.8357028.

[22] A. Jouyaeian, Q. Fan, R. Zamparette, U. Ausserlechner, M. Motz, and K. A. A. Makinwa, "A Hybrid Magnetic Current Sensor With a Multiplexed Ripple-Reduction Loop," IEEE Journal of Solid-State Circuits, vol. 58, no. 10, pp. 2874–2882, 2023, doi: 10.1109/JSSC.2023.3273389.

[23] Keysight Technologies, Impedance Measurement Handbook: A Guide to Measurement Technology and Techniques, 6th Edition, 2024.

[24] G. Antonini, A. E. Ruehli, D. Romano, and F. Loreto, "The Partial Elements Equivalent Circuit Method: The State Of The Art," IEEE Transactions on Electromagnetic Compatibility, 2023, doi: 10.1109/TEMC.2023.3302700.

[25] J. Ekman, Electromagnetic Modeling Using the Partial Element Equivalent Circuit Method, PhD dissertation, Luleå tekniska universitet, Luleå, 2003.

[26] E. Grover and F. Grover, Inductance Calculations: Working Formulas and Tables, Mathematics of Computation, vol. 18, 1964, doi: 10.2307/2003443.

[27] E. B. Rosa, "The Self and Mutual Inductances of Linear Conductors," Bulletin of the Bureau of Standards, vol. 4, no. 2, pp. 301–344, 1908, doi: 10.6028/bulletin.088.

[28] C. Hoer and C. Love, "Exact Inductance Equations for Rectangular Conductors with Applications to More Complicated Geometries," Journal of Research of the National Bureau of Standards, Section C: Engineering and Instrumentation, vol. 69, pp. 127–137, 1965, doi: 10.6028/jres.069c.016.

[29] A. Ruehli, "Inductance Calculations in a Complex Integrated Circuit Environment," IBM Journal of Research and Development, vol. 9, pp. 470–481, 1972, doi: 10.1147/rd.165.0470.

[30] M. Stumpf, F. Loreto, G. Pettanice, and G. Antonini, "Partial-inductance Retarded Partial Coefficients: Their Exact Computation Based on the Cagniard–DeHoop Technique," Engineering Analysis with Boundary Elements, vol. 149, pp. 86–91, 2023, doi: 10.1016/j.enganabound.2023.01.008.

[31] M. Kazimierczuk, High-Frequency Magnetic Components, 2nd Edition, 2013, doi: 10.1002/9781118717806.